

# UC Irvine

## UC Irvine Previously Published Works

### Title

Mechanical characterization of a unidirectional pultruded composite lamina using micromechanics and numerical homogenization

### Permalink

<https://escholarship.org/uc/item/9td0q01k>

### Authors

Xin, Haohui  
Mosallam, Ayman  
Liu, Yuqing  
[et al.](#)

### Publication Date

2019-08-01

### DOI

10.1016/j.conbuildmat.2019.04.191

Peer reviewed

# **MECHANICAL CHARACTERIZATION OF UNIDIRECTIONAL PULTRUDED COMPOSITE LAMINA USING MICRO- MECHANICS AND COMPUTATIONAL HOMOGENIZATION**

Haohui Xin<sup>a,b</sup>, Yuqing Liu<sup>a\*</sup>, Ayman Mosallam<sup>c</sup>, Milan Veljkovic<sup>b</sup>

<sup>a</sup>Department of Bridge Engineering, Tongji University, Shanghai, China

<sup>b</sup>Faculty of Geoscience and Engineering, Delft University of Technology, Netherlands

<sup>c</sup> Department of Civil & Environment Engineering, University of California, Irvine,  
California, USA

\*E-mail: [yql@tongji.edu.cn](mailto:yql@tongji.edu.cn)

## **ABSTRACT**

Unlike the simplified procedure for characterizing conventional construction materials such as steel, mechanical characterization of pultruded composites requires a more sophisticated multi-scale analysis. This is due to several reasons including: (i) the orthotropic nature of each lamina that requires identification of several engineering constants and strength parameters and (ii) pultruded composites are not precisely laminated structures, and (iii) experimental characterization of lamina mechanical properties are tedious and expensive. In this paper, analytical and numerical homogenization methods are proposed to effectively simulate the pultruded lamina macroscopic properties. In this study, a continuum damage model was implemented via user material subroutine to model fiber failure, while the Mohr-Coulomb plastic criterion is employed to model the matrix damage and the cohesive surfaces reflecting the relationship between traction and displacement in order to simulate the fiber-matrix interface. Tensile, compressive, and shear performances were experimentally studied to validate the results of the proposed theoretical and numerical approaches. Results of this study indicated that both theoretical, numerical prediction values agreed well with

experimental verification results indicating that the proposed methodologies can provide a reference for structural design and construction of pultruded composite structures.

**Keywords:** Pultruded unidirectional GFRP lamina, micro-mechanic analysis, numerical homogenization, engineering constants, Mohr-Coulomb plastic criterion.

## 1. INTRODUCTION

Deterioration of existing structures built with traditional materials such as concrete, steel and timber is considered to be a major challenge for civil engineers. Fiber Reinforced Polymer (FRP) composites are one of the promising alternative materials that potentially can solve this problem with its unique features such as its high-strength-to-weight ratio, and high resistance to harsh environments [1–5]. One of the popular types of composites that have been used by civil engineers for the past three decades or so is manufactured through the pultrusion continuous manufacturing process. Pultruded glass fiber reinforced polymer (GFRP) composites could meet the established design criteria with reasonable cost and are often recommended for newly constructed bridges and buildings [6–9]. Typical pultruded composites profiles used in civil engineering application includes I- and H-shaped girders [1,2], double web beam [10], GFRP-concrete hybrid decks [3,4,11] and modular bridge decks [12,13].

Different from traditional regulated specifications of reinforced concrete and steel, GFRP composites are inhomogeneous, anisotropic and viscoelastic and should be viewed and analyzed at different levels and on different scales (micro-mechanics and macro-mechanics).

The importance of adopting a multi-scale analysis in determining mechanical properties of

pultruded GFRP laminates has been recommended in previous studies [e.g. 12, 13]. Although several investigations on carbon fiber reinforced polymer (CFRP) for aerospace structures were conducted, results and outcomes of such studies are not generally applicable to pultruded composites that are commonly used in construction applications. One of the known difficulties in accurately analyzing and modeling pultruded composites [14] is that pultruded composites are not precisely laminated structures due to the nature of the pultrusion process. For this reason, analytical modeling that considers the nature of composites produced by the pultrusion manufacturing process is required in order to accurately identify such properties. Details for calculating lamina thickness, laminates fiber volume fraction and engineering constants of each lamina were reported previously by authors [12, 13]. In addition, and in order to accurately obtain lamina strength, laboratory tests to characterize the strength of unidirectional lamina strength are needed. However, experimental approach is usually impractical due to several reasons including: (i) each lamina is orthotropic that requires measuring several strength parameters including: longitudinal tensile strength,  $X_T$ , longitudinal compressive strength,  $X_C$ , transverse tensile strength,  $Y_T$ , transverse compressive strength,  $Y_C$ , and in-plane shear strength,  $S$ , (ii) as stated earlier, pultruded composites are not precisely laminated in the true sense due to the nature of the pultrusion process and it is physically almost impossible to extract experimentally mechanical properties of an individual lamina (refer to Fig. 1). For this reason, micromechanics approach, the technique used to obtain approximate values of composite material, are adopted in this study, where accurate homogenization models is used to predict the equivalent properties of pultruded composites. Micromechanics models can be classified into analytical and numerical. The analytical methods include: empirical, semi-empirical, and strictly-analytical mode. Many analytical

techniques of homogenization are based on equivalent Eigen-strain method [15]. The Reuss model [15] (also called *rule of mixtures*), assumes that the strain tensors in the fiber, matrix and composites are the same. The longitudinal elastic modulus  $E_1$  and longitudinal Poisson's ratio  $\nu_{12}$  are derived and computed this way in the rule of mixtures formulas. The *Voigt* model (also called *inverse rule of mixtures*), assumes that the stress tensors in the fiber, matrix and composite are the same. The transverse elastic modulus  $E_2$  and in-plane shear modulus  $G_{12}$  etc. are derived and computed this way in the rule of mixtures formulas. Considering initial imperfections, the formulas of *rule of mixtures* were improved by introducing several empirical parameters [16]. If the composite could be approximated as having periodic microstructure, then Fourier series could be used to estimate all the components of the stiffness tensor of a composite. Explicit formulas for a composite reinforced by long circular cylindrical fibers, which are periodically arranged in a square array, are adopted by Barbero et al. [17]. In addition to elastic engineering constants prediction, the rule of mixtures formula [15, 18, 19] was used to predict lamina's longitudinal tensile strength  $X_T$  and longitudinal compressive strength  $X_C$ , where it assumed that the fibers and the matrix behaved linearly up to failure and the fibers were brittle and stiff with respect to the matrix, leading that the longitudinal tensile strength is controlled by the fiber strength. The longitudinal compressive failure mode [15, 18] was also assumed to be triggered by fiber micro-buckling when individual fibers buckle inside the matrix. The transverse tensile strength of composites [18, 20] is controlled by matrix ultimate strength and it is lower than the matrix strength by a factor (SRF) known as strength-reduction factor, which depends on the relative properties of the fibers and the matrix and their volume fractions. The transverse compressive strength could be obtained by the *strain-magnification factor* method [21, 22] or

empirical formulas [23, 24]. Compared with analytical micromechanics formulations [25], numerical homogenization simulation could accurately consider the geometry and spatial distribution of the phases, and also could precisely estimate the propagation of damage to accurately predict the failure strength. Numerical homogenization method [26] is emerging methodology and is considered to be an effective modeling tool to analyze advanced composites, where the macroscopic properties of lamina could be acquired by means of the numerical modeling of deformation and failure of microstructure model, a representative volume element (RVE). Results of several research studies on nonlinear mechanical response of FRP lamina simulation have been reported. For example, Gonzalez and LLorca [25] analyzed the mechanical response of a unidirectional FRP subjected to transverse compression. The results showed that transverse compression behaviors of unidirectional FRP were mainly controlled by interface strength and the matrix yield strength while the failure modes were controlled by by the nucleation of interface cracks or by the formation of matrix shear bands. Vaughan and McCarthy [27] investigate the effect of fiber–matrix debonding and thermal residual stress on the transverse damage behavior of unidirectional FRP. Results of their study indicated that the fiber-matrix interface strongly affected the transverse strength and that the interfacial strength is one of the major controlling factors of the overall transverse strength. Soni et al. [28] developed a three-dimensional micromechanical finite element model to predict mechanical behavior and damage response of composite laminates, where the macroscopic stress-strain fields were obtained using Gauss’s theorem, in conjunction with the Hill-Mandal strain energy equivalence principle. The predicted results from the proposed model, which could be used to study effects of matrix friction angle and cohesive strength of the fiber-matrix interface on global material

response, and also could be used to predict initiation and propagation of the fiber-matrix interfacial decohesion and propagation at every point in the laminate, were found to be in good agreement with experimental results. Romanowicz [29] employed the numerical homogenization methods to predict the strength of unidirectional FRP lamina under a combination of the transverse compression and axial tension. The failure modes mainly presented fiber breakage, fiber/matrix debonding and matrix plastic deformation. The proposed model is verified against an analytical solution and experimental data. Results showed that the numerical results agreed better with experimental data than analytical model. Melro et al. [30, 31] used a pressure-dependent, elasto-plastic thermodynamically consistent damage mode to simulate the matrix and used cohesive elements to model the interface between matrix and fibers. Their results showed that damage initiation is mainly due to interfacial damage under both transverse tension and shear loadings and that the damage initiation under longitudinal shear load is mainly due to the damage of epoxy matrix. Ullah et al. [32] developed a computational homogenization framework to predict the nonlinear mechanical response of FRP composites. The accuracy and performance of the computational framework are demonstrated with a variety of numerical examples.

In order to extend the use of pultruded GFRP profiles in bridge engineering and provide basic design data of pultruded unidirectional GFRP lamina, analytical and numerical homogenization methods were used to effectively model the macroscopic properties of lamina. Continuum damage model implemented via user material subroutine is employed to simulate fiber failure, Mohr-Coulomb plastic criterion is employed to simulate the matrix damage and the cohesive surfaces reflecting the relationship between traction and displacement at the interface were employed to simulate the fiber-matrix interface. Tensile

performance, compressive performance and shear performance have been experimentally studied to validate the theoretical and numerical results.

## **2. ANALYTICAL MICROMECHANICS EVALUATION**

It is quite difficult and expensive to fabricate pultruded lamina accompany with the pultrusion profiles fabrication for the ASTM materials characterization standard tests in order to precisely obtain elastic engineering constants and strengths of each lamina. Based on information obtained from in-depth literature review conducted in this study, it is believed that there is a dearth of references involving pultruded FRP profiles in civil engineering application with multiscale prediction in both engineering constants and ultimate capacity.

### **2.1 Lamina Engineering Constants**

The engineering constants of a unidirectional lamina include longitudinal elastic modulus  $E_1$ , transverse elastic modulus  $E_2$ , in-plane shear modulus  $G_{12}$ , transverse shear modulus  $G_{23}$ , longitudinal Poisson's ratio  $\nu_{12}$  and transverse Poisson's ratio  $\nu_{23}$ . The detailed equations to predict lamina engineering constants were listed in Appendix A.

### **2.2 Lamina Ultimate Strength**

The ultimate strength of a pultruded unidirectional lamina includes longitudinal tensile strength  $F_{1t}$ , transverse tensile strength  $F_{2t}$ , longitudinal compressive strength  $F_{1c}$ , transverse compressive strength  $F_{2c}$  and in-plane shear strength  $S$ . Detailed equations to predict ultimate strength were listed in Appendix B. It is also noted that the purpose of predicted strength is to provide initial coarse reference in the finite element simulation in the fact that the constitutive law of sub-materials and interface between sub-materials were much complicated.



### 3. COMPUTATIONAL HOMOGENIZATION

As compared with analytical micromechanics formulations [25], numerical homogenization simulation could accurately consider the geometry and spatial distribution of the phases, and also could precisely estimate the propagation of damage to accurately predict the failure strength.

#### 3.1 Computational Homogenization and Periodic Boundary Condition

The link between micro-scale and macro-scale behavior could be established based on Hill-Mandel computational Homogenization method. The macro-scale Cauchy stress  $\bar{\sigma}_{ij}$  is obtained by averaging the micro scale Cauchy stress,  $\sigma_{ij}$ , in the unit cell domain, expressed as Eq. 1. [26]:

$$\bar{\sigma}_{ij} = \frac{1}{|\Theta|} \int_{\Theta} \sigma_{ij} d\Theta \quad (1)$$

where:  $\bar{\sigma}_{ij}$  is the macro-scale Cauchy stress,  $\sigma_{ij}$  is the micro-scale Cauchy stress,  $\Theta$  is the domain of the unit cell. The unit cell problem could be solved for the leading order translation-free micro-scale displacement. The micro-scale displacement  $u_i^f(x, y)$  is expressed in the following form [26]:

$$u_i^f(x, y) = \varepsilon_{ij}^c y_j + u_i^{(1)}(x, y) \quad (2)$$

where:  $x$  is the macro-scale position vector in the macro-scale domain,  $y$  is the micro-scale position vector in the unit cell domain;  $\varepsilon_{ij}^c$  is the strain tensors in the macro-scale domain,

$u_i^{(1)}(x, y)$  is the perturbation displacement of the micro-scale.

If two nodes,  $M$  and  $S$ , located at the opposite faces of the RVE model, with  $M$  and  $S$  being the master and slave nodes respectively. The fine scale displacement at the two nodes are given as [26] Eq. (3) and Eq. (4) based on expression in Eq.(2).

$$u_i^f(x, y^M) = \varepsilon_{ij}^c y_j^M + u_i^{(1)}(x, y_j^M) \quad (3)$$

$$u_i^f(x, y^S) = \varepsilon_{ij}^c y_j^S + u_i^{(1)}(x, y_j^S) \quad (4)$$

where:  $y^M$ , and  $y^S$  are the fine-scale coordinates. Considering the periodic boundary conditions [26] in the unit cell domain, gives:

$$u_i^{(1)}(x, y_j^M) = u_i^{(1)}(x, y_j^S) \quad (5)$$

Thus, above two equations yield to the following relation [26]:

$$u_i^f(x, y_j^M) - u_i^f(x, y_j^S) = \varepsilon_{ij}^c (y_j^M - y_j^S) \quad (6)$$

This could be implemented by so called “mixed boundary conditions” via constraint equations, is expressed by the following equations [26,33]:

$$\int_{\partial\Theta_y} (u_i^f(x, y) - \varepsilon_{ik}^c y_k) N_j^\ominus d\gamma_y = 0 \quad (7)$$

$$|u_i^f(x, y) - \varepsilon_{ik}^c y_k| N_j^\ominus \leq Tol \quad (8)$$

where:  $N_j^\ominus$  is the unit normal to the unit cell boundary  $\partial\Theta_y$ .

### 3.2 Material Constitutive Model

Typical RVE model in the case of unidirectional GFRP composites employed in this paper is shown in Fig. 2, that consists of a fiber embedded in a matrix polymer. The macro-scale GFRP material behavior could be obtained by averaging micro-scale stress distribution and

considering individual sub-materials components constitutive law and fiber-matrix interface de-bonding. Each constitutive model of sub-material is detailed explained as below section.

**3.2.1 Fibers:** Continuum damage material model was implemented via the user-material subroutine UMAT of ABAQUS/Standard [34] to simulate the fiber damage. The stress and strain relationship [12] was expressed as follows:

$$\sigma_{ij} = (1 - w) L_{ijkl} \varepsilon_{kl} \quad (9)$$

where:  $w$  is the damage variable. Once a damage initiation is detected, further loading will cause degradation of material stiffness. The reduction of the stiffness coefficients depended on damage variables. The evolution of damage variable,  $w$ , is assumed to be governed by equivalent strain  $\hat{\varepsilon}$ . Now, considering the brittle nature of glass fibers, the glass fibers is assumed to be fully damaged when the equivalent strain,  $\hat{\varepsilon}$ , increases to a value larger than the defined strain threshold value  ${}^t\varepsilon_f^u$ . The damage variable is given as following relationship:

$$Y(\hat{\varepsilon}) = \begin{cases} 0 & \hat{\varepsilon} < {}^t\varepsilon_f^u \\ w_{\max} & \hat{\varepsilon} \geq {}^t\varepsilon_f^u \end{cases} \quad (10)$$

where:  $w_{\max}$  is the maximum value of damage variable and is assumed to be 0.999 in this manuscript to avoid convergence problems. The equivalent strain,  $\hat{\varepsilon}$ , is defined as follows:

$$\hat{\varepsilon} = \sqrt{\frac{2}{3} \sum_{i=1}^3 \langle \bar{\varepsilon}_i \rangle^2} \quad (11)$$

where:  $\bar{\varepsilon}_i$  is the principal strain in each direction. Note that the shear strain is zero in the principal strain coordinate. The operator “ $\langle \rangle$ ” is defined in order to consider the difference between tensile damage and compressive damage of glass fibers. The effective principal

strain,  $\langle \bar{\varepsilon}_i \rangle$ , in each direction is given as following relationship:

$$\langle \bar{\varepsilon}_i \rangle = \begin{cases} \bar{\varepsilon} & \bar{\varepsilon}_i \geq 0 \\ \chi \bar{\varepsilon} & \bar{\varepsilon}_i < 0 \end{cases} \quad (12)$$

where: the material parameter  $\chi$  is defined as the ratio of the ultimate tensile strain to the ultimate compressive strain.

$$\chi = \frac{{}^t \varepsilon_f^u}{{}^c \varepsilon_f^u} \cong \frac{{}^t \sigma_f^u}{{}^c \sigma_f^u} \quad (13)$$

where:  ${}^t \sigma_f^u$  and  ${}^c \sigma_f^u$  is ultimate tensile and compressive strength of fibers.

The yield function that predicts damage initiation of glass fibers is expressed by the following relation:

$$g(\hat{\varepsilon}, r) = \hat{\varepsilon} - r \leq 0 \quad (14)$$

The loading functions obey the loading-unloading conditions of the Karush–Kuhn–Tucker conditions, and are expressed in the following form [14]:

$$\dot{w} \geq 0, \quad g(\hat{\varepsilon}, r) \leq 0, \quad \dot{w} g(\hat{\varepsilon}, r) = 0 \quad (15)$$

Materials models with softening behavior and stiffness degradation generally have convergence difficulties in implicit finite element method. In order to alleviate convergence difficulties, a viscous regularization scheme is adopted, and a viscous damage variable is defined by the evolution equations [14]:

$$\dot{w}^v = \frac{1}{\eta} (w - w^v) \quad (16)$$

where:  $\eta$  is a viscosity coefficient representing the relaxation time of the viscous system

and  $w^v$  denotes regularized damage variable.

The finite element equations obtained for this model by discretizing the virtual work equations are in general nonlinear, and the Newton–Raphson technique is used to solve the resulting system of nonlinear equations in ABAQUS [34]. It is important to note that the material tangent constitutive tensor is computed correctly to ensure robustness of the Newton–Raphson method. The material tangent constitutive tensor could be computed from the following equation:

$$\frac{\partial \sigma_{ij}}{\partial \varepsilon_{kl}} = (1 - w^v) L_{ijkl} \quad (17)$$

The detailed implementation algorithm is summarized in Table 1.

**3.2.2 Polymer Matrix:** The polymeric matrix was assumed to be behaved as isotropic materials. The plastic behavior of polymer matrix was assumed to be governed by the Mohr-Coulomb criterion [34,35]. The Mohr-Coulomb criterion assumes that the yielding happens when the shear stress along one specific plane reaches a critical value, which is related to the normal stress  $\sigma$ . It is expressed as:

$$\tau = c - \sigma \tan \phi \quad (18)$$

where:  $c$  stands for the cohesion of the matrix materials,  $\phi$  stands for the friction angle of the matrix materials. The cohesion,  $c$ , stands for the failure stress under pure shear while the friction angle  $\phi$  is used to consider the effects of the hydrostatic stress on yield stress.

The values of both material parameters could be determined from its tensile and compressive strengths,  $\sigma_{mt}$  and  $\sigma_{mc}$  expressions as follow:

$$\sigma_{mt} = 2c \frac{\cos \phi}{1 + \sin \phi} \quad (19)$$

$$\sigma_{mc} = 2c \frac{\cos \phi}{1 - \sin \phi} \quad (20)$$

The Mohr-Coulomb yield surface can then be expressed as [34]:

$$F = R_{mc}q - p \tan \phi - c = 0 \quad (21)$$

where:

$p$  is the hydrostatic stress:

$$p = -\frac{1}{3} \sigma_{ij} \delta_{ij} \quad (22)$$

$q$  is the Mises equivalent stress:

$$q = \sqrt{\frac{3}{2} S_{ij} S_{ij}} \quad (23)$$

$S_{ij}$  is the deviatoric stress defined as:

$$S_{ij} = \sigma_{ij} - p \delta_{ij} \quad (24)$$

$R_{mc}$  is defined as the Mohr-Coulomb deviatoric stress measure defined as [34]:

$$R_{mc} = \frac{1}{\sqrt{3} \cos \phi} \sin \left( \Theta + \frac{\pi}{3} \right) + \frac{1}{3} \cos \left( \Theta + \frac{\pi}{3} \right) \tan \phi \quad (25)$$

$\Theta$  is the deviatoric polar angle defined as:

$$\cos(3\Theta) = \left( \frac{r}{q} \right)^3 \quad (26)$$

$r$  is the third invariant of deviatoric stress:

$$r = \left( \frac{9}{2} S_{ij} \cdot S_{ij} : S_{ij} \right)^{1/3} \quad (27)$$

A non-associated flow rule was employed to compute the directions of plastic strain in the stress space in ABAQUS [34]. The plastic strain is given in the following expressions:

$$\dot{\varepsilon}_{ij}^p = \frac{\lambda}{g} \frac{\partial G}{\partial \sigma_{ij}} \quad (28)$$

$$g = \frac{1}{c} \frac{\sigma_{ij} \partial G}{\partial \sigma_{ij}} \quad (29)$$

The flow potential,  $G$ , is assumed as hyperbolic function [34]:

$$G = \sqrt{(\xi c_0 \tan \psi)^2 + (R_{mv} q)^2} - p \tan \psi \quad (30)$$

$$R_{mv} = \frac{4(1-e^2)\cos^2 \Theta + (2e-1)^2}{2(1-e^2)\cos^2 \Theta + (2e-1)\sqrt{4(1-e^2)\cos^2 \Theta + 5e^2 - 4e}} \frac{3 - \sin \phi}{6 \cos \phi} \quad (31)$$

$$e = \frac{3 - \sin \phi}{3 + \sin \phi} \quad (32)$$

where:  $\psi$  is dilation angle,  $\xi$  is the meridional eccentricity parameters,  $c_0$  is the initial cohesion when the plastic strain is zero,  $e$  is the parameter of the deviatoric eccentricity.

**3.2.3 Fiber-Matrix Interface:** The cohesive surfaces reflecting the relationship between traction and displacement at the interface were employed to simulate the fiber-matrix interface. As is shown in Fig. (3-a), the bilinear traction-separation model, which assumed to be linear elastic (point “a”) followed by the damage initiation (point “b”), evolution of damage (point “c”), and finally the fully damaged state (point “d”), is employed in this paper. In the elastic stage [12,13], the traction increased linearly along the displacement with an initial slope of  $K_0$ . At point “b”, the damage of cohesive element is initiated. The cohesive element is always subjected to complicated loading condition; the quadratic stress failure criterion [34] is used to evaluate the initial damage, as is shown in Fig. (3-b).

$$\left\{ \frac{\langle t_n \rangle}{t_n^0} \right\}^2 + \left\{ \frac{t_s}{t_s^0} \right\}^2 + \left\{ \frac{t_t}{t_t^0} \right\}^2 = 1 \quad (33)$$

where:  $t_n$ ,  $t_s$  and  $t_t$  are traction components related to pure modes *I*, *II* and *III*,  $t_n^0$ ,  $t_s^0$  and  $t_t^0$  are interfacial strength of pure modes *I*, *II* and *III*.

In the damage evolution period, the interfacial stiffness degraded from initial  $K_0$  to  $(1-d)K_0$ , where  $d$  is a damaged variable. The Benzeggagh-Kenane fracture criterion (BK Law) described in Eq. (34) [34, 36] is particularly used to predict damage propagation of mixed-mode loadings in terms of the critical fracture energies during deformation purely along the first and the second shear directions are the same.

$$G^C = G_n^C + (G_s^C - G_n^C) \left\{ \frac{G_s + G_t}{G_n + G_s + G_t} \right\}^\eta \quad (34)$$

where:  $G_n$ ,  $G_s$ , and  $G_t$  are the corresponding energy release rates under pure modes *I*, *II*, and *III*, the additional subscript “*C*” denotes critical case, which can be determined based on a standard fracture toughness test and  $\eta$  is a material parameter.

## 4 EXPERIMENTAL PROGRAMS AND RESULTS

### 4.1 Properties of Fiber and Resin

Tables 2 and 3 present a summary of mechanical properties of E-glass fibers and epoxy resin, respectively [37].

### 4.2 Processing Method

As shown in Fig. 4, a typical pultrusion production line consists mainly of the following components [38]: (i) roving/fabric stacked on creels, (ii) pre-forming guide plate, (iii) resin impregnator, (iv) forming & curing die, and (v) a pulling system and cutting system. Glass fibers rovings are guided by a pre-forming plate from a creel into a resin impregnation tank for wetting the reinforcements with polymeric matrix. The pre-forming guide plate guides



positions of reinforcements in the designed locations in the cross section of profiles. The wetted reinforcements are then travels through heated die to cure epoxy resin drawn by pulling system. The resin matrix progressively changes from liquid to gel and finally to solid. After performing and shaping, the composites are pulled out and cut off based on required length.

### **4.3 Density and Fiber Volume Fraction Tests**

In this study, three specimens with nominal dimensions of 25.0 mm × 25.0 mm × 4.0 mm were fabricated to investigate the fiber fraction based on calcination methods [39] and density [40]. The specimens were weighed to acquire composite destiny before burning in an incinerator. After burning, the remaining consists only of fiber that was weighed to determine the fiber volume fraction of each specimen. Table 4 presents a summary of results of these tests. As shown in this table, the average density of the pultruded composite lamina is 1920.10 kg/m<sup>3</sup> with an average fiber volume fraction of 56.2%.

### **4.4 Test Specimens**

The tensile performance, Poisson's ratio, compressive performance and in-plane shear performance of pultruded lamina have been experimentally investigated. As shown in Fig.5, five specimens were tested under tension load parallel to fiber direction and five specimens were tested under tension load perpendicular to fiber direction in order to measure the ultimate tensile strength, elastic modulus and the Poisson's ratio based on procedures described in reference [41]. The typical dimensions of the longitudinal tensile specimens are 230.0 mm× 15.00 ×4.0 mm, while the dimensions of the transverse tensile specimens is 170.0 mm×25.0 mm×4.0 mm. In addition, five specimens were tested under compression along the fiber direction and another five specimens perpendiculars to the fiber direction [42]

were also tested under compression (refer to Fig. 6). The average dimension of the compressive specimens is 110.0 mm×8.7.0 mm×4.0 mm with an effective compressive length of 10.0 mm. A total of five specimens were also prepared based on procedures described in reference [43] in to measure the in-plane shear strength and modulus of each specimen (refer to Fig. 7). The average dimension of the in-plane shear specimen is 76.0 mm×56.0 mm×4.0 mm (see Fig. 7). The loads and displacements were measured by a calibrated universal testing machine (UTM) load cell and displacement sensor, while strains were measured using strain gauges during loading process.

#### **4.5 Experimental Results**

Table 5 presents a summary of experimental results. In this table,  $SD$  is the standard deviation,  $COV$  is the coefficient of variability,  $E_{av}$  is the average elastic modulus,  $E_{95\%}$  is the elastic modulus with 95% reliability,  $U_{av}$  is the average ultimate strength, and  $U_{95\%}$  is the ultimate strength with 95% reliability.

The average longitudinal tensile strength, transverse tensile strength, longitudinal compressive stress, transverse compressive stress, and the in-plane shear stresses obtained from the tests are 1146.03MPa, 47.45MPa, 1014.34MPa, 168.40MPa and 48.50MPa, respectively. The average experimental values of longitudinal tensile elastic modulus, transverse tensile elastic modulus, longitudinal compressive elastic modulus, transverse compressive elastic modulus and in-plane shear modulus are 47.17GPa, 16.18GPa, 55.02GPa, 16.74GPa and 5.04GPa, respectively. Test results also indicated that the average longitudinal and transverse Poisson's ratio are 0.265 and 0.114, respectively. Test results

showed that the experimental value of the in-plane shear strength is smaller than the predicted value obtained in previous studies [12–14]. This variation may be attributed to the fact that the behavior of woven reinforced lamina is different from unidirectional GFRP lamina. For this reason, further research is underway to gain in-depth understanding of the in-plane shear behavior of such laminates.

#### 4.6 Resistance Factor

The load and resistance factor design (LRFD) protocol is commonly adopted in the bridge engineering. According to LRFD design method, the resistance of the structure and the applied loads are considered separately. The design should satisfy following inequality [44].

$$\Phi F > \alpha_D L_D + \psi \sum_{j=1}^{N_L} \alpha_j L_j \quad (2)$$

where:  $F$  is material strength,  $\Phi$  is resistance factor,  $\alpha_D$  is dead load factor,  $L_D$  is dead load,  $\alpha_j$  is live load factors,  $L_j$  is other loads including live, pressure, thermal, acceleration etc., and  $N_L$  is number of other types of design loads.

Now, assuming that the applied stress is deterministic, the resistance factor could be obtained for a given reliability relation as follows [15]:

$$\Phi = \frac{\mu_F + z\bar{\omega}_F}{\mu_F} = 1 + zC_F \leq 1 \quad (3)$$

where:  $\mu_F$  is average strength,  $\bar{\omega}_F$  is standard deviation (SD),  $C_F$  is coefficient of variability (COV),  $z$  is variable in terms of standard normal Gaussian probability density function.

The results of resistance factors are summarized in Table 6. If the required reliability is

95%, the resistance factor of the elastic modulus will then falls between 0.84 and 0.90, and the corresponding ultimate strength resistance factor will fall in the range of 0.82 to 0.97. In case that the required reliability is 99%, the elastic modulus resistance factor of will fall between 0.77 and 0.86 while the ultimate strength resistance factor falls within a range between 0.74 to 0.95. Therefore, an ultimate strength resistance factor of 0.8 for 95% reliability and 0.7 for 99% reliability on the safety side is adopted.

## 5. COMPARISONS AND DISCUSSION

### 5.1 Engineering Constants Comparisons

Using Eq. A.1.1 of Appendix A, the predicted density of composites is  $1,946.8 \text{ kg/m}^3$ , and the difference between theoretical value and experimental value is within 3%.

Figure 8, shows a comparison between analytical, numerical and experimental engineering constants results. It is noted that all the predicted values of both the longitudinal elastic modulus  $E_l$  and longitudinal Poisson's ratio,  $\nu_{l2}$ , agreed well with the average experimental results and that the test results fall within 95% reliability, with a difference of about 10%. For the transverse elastic modulus,  $E_2$ , the predicted value obtained from the *improved* roles of mixture and numerical homogenization agreed well with the average experimental results and the test results fall within a 95% reliability. However, predicted values obtained from other methods tended to be smaller than average test results. With respect to the in-plane shear modulus, the predicted value, except of the case of roles of mixture, agreed well with both the average experimental results that test results fall within 95% reliability.

### 5.2 Ultimate Strength Comparisons

**5.2.1 Longitudinal Tensile Strength:** Figure 9 shows comparisons between experimental

and theoretical ultimate strength and stress-strain relationship for specimens subjected to longitudinal tensile loading. As shown in Fig. 9-a, the predicted ultimate strength values obtained from the “roles of mixture” equations (Eqn. B.1.1 of Appendix B), and the “numerical homogenization” approach both agreed well with experimental results. As shown in this figure, the predicted value obtained from the “roles of mixture” approach is 10% larger than the average experimental results but is about 14% larger than the experimental results with 95% reliability. In addition, the difference between predicted results obtained from “numerical homogenization” approach and corresponding experimental results is within 7%. Also, theoretical stress-strain relationship for specimens subjected to longitudinal tensile loading calculated using “numerical homogenization” agreed well with experimental values (refer to Fig. 9-b).

Figure 10 presents the Mises stress, equivalent plastic strain, and damage distributions in the unit cell domain under longitudinal tensile loading. As shown in Fig. 10-a, in the elastic stage, the fibers Mises stress are generally much larger than the matrix stresses due to elastic moduli differences. One can also see that plastic strains developed gradually in the matrix phase and that fiber-matrix de-bonding developed gradually as the longitudinal load increased. The Mises stress has a periodic distribution in both the elastic and plastic stages under longitudinal tensile loading, indicating that the unit cell was modeled with correct periodic boundary conditions based on Eqns. (7) and (8). As shown in Fig.10-b, the longitudinal load reached its maximum when the fiber damage initiated, and this failure agreed well with the basic assumption of *role of mixtures* approach presented in Eqn. B.1.1 of Appendix B.

**5.2.2 Longitudinal compressive strength:** Figure 11 presents comparisons between

theoretical and experimental ultimate strength and stress-strain relationships for specimens subjected to longitudinal compressive loads. By assuming the correction factor  $\beta$  to be 1.16 in the “roles of mixture” equation (Eqn. B.2.1 in Appendix B), the differences between predicted and experimental results are within 10%. If a correction factor  $\beta$  is assumed to be 0.28 in the “fiber buckling method” (Eqn. B.2.2 of Appendix B), the predicted value would agree well with test results. The predicted result of the “improved fiber buckling method” (Eqn. B.2.3 of Appendix B) agrees well with experimental results if a fiber misalignment standard deviation of  $\alpha_\sigma = 1.15$  is assumed. Also, results showed that the predicted value obtained from the “numerical homogenization” approach is 14% less than the average experimental results and 6% less than the experimental results with 95% reliability. As shown in Fig. 11-b, the predicted stress-strain relationship based on “numerical homogenization” method generally agrees well with test results.

Figure 12 presented Mises stress, equivalent plastic strain and damage distributions in the unit cell domain under longitudinal compressive loading. As is shown in Fig. 12-a, in the elastic stage, elastic modulus of fiber is much larger than the matrix leading to that fiber distributed larger Mises stress. The Mises stress of both fiber and matrix presented periodic distribution in both elastic stage and plastic stage. Obvious plastic strain appeared in the matrix phase and fiber-matrix de-bonding occurred in the plastic stage. As is shown in Fig. 12-b, de-bonding between fiber and matrix interface and damage of fiber led to final failure under longitudinal compressive loading.

**5.2.3 Transverse tensile strength:** Figure 13 presented ultimate strength and stress-strain relationship comparisons under transverse tensile loading. The predicted value from stress concentration method in Eqn.B.3.1 in Appendix B, with concentration factor proposed by

Agarwal [18] (Eqn. B.3.2 in Appendix B) is less than experimental results while the difference between predicted value from stress concentration method with concentration factor proposed by Huang [20] (Eqn. B.3.3 in Appendix B) is within 10% under assuming bridge factor  $\beta$  as 0.70. The predicted value based on linear fracture mechanics method (Eqn. B.3.6 of Appendix B) agreed well with test results if mode I critical fracture energy  $G_{Ic}$  is assumed to be 140.0 J/m<sup>2</sup>. Now, assuming  $V_v$  to be 0.02, based on previous literature [15], the predicted value using the empirical equation is 5% larger than the average test results and 20% larger than the test results with 95% reliability. The predicted value from the “numerical homogenization” method is 1.5% less than the average experimental results and 10.5% less than the experimental results with 95% reliability. As is shown in Fig.13-b, the stress-strain relationship predicted from the “numerical homogenization” method for specimens subjected to transverse tensile loading agreed well with test values.

Figure 14 presents Mises stress, equivalent plastic strain and damage distributions in the unit cell domain under transverse tensile loading. As shown in Fig. 14-a, the Mises stress for both the fibers and the matrix exhibited periodic distribution in both the elastic stage and plastic stage. The maximum Mises stress value in the elastic stage appeared in the middle of fibers, while the maximum Mises stress in the plastic stage occurred near the interface. As shown in Fig. 14-b, de-bonding between fiber and matrix interface and damage of matrix led to final failure under transverse tensile loading. No fiber damage occurred during the transverse tensile loading, indicating that the transverse tensile behavior is mainly controlled by matrix and interface performance.

**5.2.4 Transverse compressive strength:** Figure 15 presents comparisons between theoretical and experimental values of both the ultimate strength and stress-strain relationship

for specimens subjected to transverse compressive loading. The predicted value from the “*strain amplification method*” (Eqn. B.4.1 of Appendix B) is 10% larger than the average experimental value, and is 12.5% larger than the test value with 95% reliability. However, the predicted result based on the empirical formula described in Eqn. B.4.2 of Appendix B is much less than the experimental results. On the other hand, the predicted value from the “numerical homogenization” method is 2.5% larger than the average experimental results, and 5.5% larger than the experimental results with 95% reliability. As shown in Fig. 15-b, the stress-strain relationship obtained from the “numerical homogenization” for specimens subjected to transverse compressive loading agreed well with test values.

Figure 16 presents the Mises stress, equivalent plastic strain and damage distributions in the unit cell domain under transverse compressive loading. As is shown in Fig. 16-a, the Mises stress of both fibers and matrix exhibited periodic distribution and that the maximum Mises stress appeared in the middle of fiber in both elastic stage and plastic stage. Also, Fig. 16-b shows that the damage of matrix led to the final failure under transverse compressive loading. No fiber damage occurred during the transverse compressive loading, indicating that the transverse compressive behavior is mainly controlled by matrix plasticity.

**5.2.5 Ultimate shear strength:** Figure 17 presents comparisons between the theoretical and experimental ultimate strength and stress-strain relationship for specimens subjected to in-plane shear loads. As shown in the figure, the analytical results obtained from the “fracture mechanics” methods is 1% less than than the average corresponding experimental value, and is 12.5% larger than the test value, with 95% reliability under the assumption that the mode II critical fracture energy,  $G_{2c}$ , is 220J/m<sup>2</sup>. Also, the predicted value from the “numerical



homogenization” approach is 1.2% larger than the average experimental results and is 18.5% larger than the experimental results with 95% reliability.

Figure 18 presents the Mises stresses, the equivalent plastic strain, and the damage distributions in the unit cell domain for specimens subjected to in-plane shear loads. As shown in Fig. 18-a, the maximum Mises stress appeared periodically at both the top and the bottom middle surface in the elastic stage. The stress redistributed due to material damage, and the maximum Mises stress occurred in the fiber due to matrix damage. As shown in Fig. 18-b, debonding between fiber and matrix interface and matrix damage led to final failure of specimens subjected to in-plane shear loads. Again, no fiber damage was observed during in-plane shear loading, indicating that the in-plane shear behavior is mainly controlled by matrix and interface performance.

Due to the fact that the thickness of FRP plate is quite small, it is usually difficult to define experimentally the transverse shear behavior of composites. For this reason, the *numerical homogenization* approach may provide a satisfactory reference for the transverse shear behavior of unidirectional FRP materials. Figures 19 show the numerical shear stress-strain curves. As shown in Fig. 19, one can notice a difference between the in-plane shear modulus and the transverse shear modulus (23-direction), while only a small difference is observed between the transverse shear strength (23-direction) and the in-plane shear strength (13-direction). It is commonly accepted that in case of lack of sufficient material test data, transverse shear strength of a pultruded unidirectional GFRP lamina could be assumed to be the same as its in-plane shear strength value [14]. The Mises stress, the equivalent plastic strain, and the damage distributions in the unit cell domain under transverse shear loading are presented in Fig. 20. As shown in Fig. 20-a, the maximum Mises stress periodically

appeared in the fibers near the matrix-fiber interface in both elastic and plastic stage. As shown in Fig. 20-b, damage of the matrix led to the final failure under transverse shear loading. No fiber damage occurred during in-plane shear loading, indicating that the transverse shear behavior is mainly controlled by matrix performance.

## 6. CONCLUSIONS

Analytical and numerical homogenization methods were successfully used in this study to effectively model the macroscopic properties of pultruded composite unidirectional GFRP lamina. Five identical tests of each tensile, compressive and shear performances were experimentally evaluated in order to validate the theoretical and numerical results. Based on the results of this study, the following conclusions are drawn:

- In terms of unidirectional GFRP lamina with fiber volume fraction of 56.2%, the average density is  $1920 \text{ kg/m}^3$ . Following mechanical properties are obtained:
  - The average longitudinal tensile strength is 1146 MPa,
  - The transverse tensile strength is 47 MPa,
  - The longitudinal compressive stress is 1014 MPa,
  - The transverse compressive stress is 168 MPa and
  - The in-plane shear stress is 48 MPa,
  - The average longitudinal tensile elastic modulus is 47 GPa,
  - The transverse tensile elastic modulus is 16 GPa,
  - The longitudinal compressive elastic modulus is 55 GPa,
  - The transverse compressive elastic modulus is 16 GPa
  - The in-plane shear modulus is 5 GPa

- The average longitudinal Poisson's ratio 0.265
- The transverse Poisson's ratio 0.114.
- Numerical homogenization is necessary for an accurate prediction of the non-linear behavior. The continuum damage model, implemented via user material subroutine, was employed to simulate fiber failure. Mohr-Coulomb plastic criterion was used to simulate matrix damage. The cohesive surfaces, reflecting the relationship between traction and displacement at the interface, were employed to simulate the fiber-matrix interface. The differences between numerical homogenization and average experimental results of longitudinal tensile, transverse tensile, transverse compression and in-plane shear is within 5% while the compressive strength of numerical homogenization is 14% less than the average experimental results. A good correlation between numerical homogenization results and test results was achieved.
- The damage of unidirectional GFRP lamina subjected to longitudinal tensile and compressive loads is controlled mainly by fiber damage. The transverse tensile and compressive stresses, in-plane and shear behavior of unidirectional GFRP lamina is controlled by the matrix and fiber-matrix interface damage.

## **ACKNOWLEDGMENTS**

The authors gratefully acknowledge the financial support provided by National Natural Science Foundation [Grant # 51578406] of People's Republic of China.

## **APPENDIX A: Prediction of Engineering Constants**

The engineering constants of a unidirectional lamina include longitudinal elastic modulus  $E_L$ ,

transverse elastic modulus  $E_2$ , in-plane shear modulus  $G_{12}$ , transverse shear modulus  $G_{23}$ , longitudinal Poisson's ratio  $\nu_{12}$  and transverse Poisson's ratio  $\nu_{23}$ .

**A.1 Roles of Mixtures:** All engineering constants could be approximated based on roles of mixtures [19] as follows:

$$\rho_c = \rho_f V_f + \rho_m V_m \quad \text{A.1.1}$$

$$E_1 = E_{f1} V_f + E_m V_m \quad \text{A.1.2}$$

$$E_2 = \frac{E_{f2} E_m}{E_m V_f + E_{f2} V_m} \quad \text{A.1.3}$$

$$G_{12} = \frac{G_{f12} G_m}{G_m V_f + G_{f12} V_m} \quad \text{A.1.4}$$

$$\nu_{12} = \nu_f V_f + \nu_m V_m \quad \text{A.1.5}$$

where:  $\rho_f$  is density of fiber,  $\rho_m$  is density of resin,  $E_{f1}$  is longitudinal elastic modulus of fiber,  $E_{f2}$  is transverse elastic modulus of fiber,  $V_f$  is fiber volume fraction,  $\nu_f$  is Poisson's ratio of fiber,  $E_m$  is elastic modulus of matrix,  $V_m$  is resin volume fraction,  $\nu_m$  is Poisson's ratio of resin.  $G_f$  is shear modulus of fiber,  $G_m$  is shear modulus of resin.

**A.2 Improved Roles of Mixtures:** To account for initial imperfections, the formulations of roles of mixture were improved as following [16]:

$$E_1 = E_{f1} V_f + E_m V_m \quad \text{A.2.1}$$

$$E_2 = E_3 = \frac{E_{f2} E_m [V_f + \eta_2 V_m]}{E_m V_f + E_{f2} \eta_2 V_m} \quad \text{A.2.2}$$

$$\eta_2 = \frac{0.2}{1-\nu_m} \left( 1.1 - \sqrt{\frac{E_m}{E_f} + \frac{3.5 E_m}{E_f}} \right) (1 + 0.22 V_f) \quad \text{A.2.3}$$

$$G_{12} = G_{13} = \frac{G_f G_m [V_f + \eta_{12} V_m]}{G_m V_f + G_f \eta_{12} V_m} \quad \text{A.2.4}$$

$$\eta_{12} = 0.28 + \sqrt{\frac{E_m}{E_f}} \quad \text{A.2.5}$$

$$G_{23} = \frac{G_f G_m (V_f + \eta_{23} V_m)}{G_m V_f + G_f \eta_{23} V_m} \quad \text{A.2.6}$$

$$\eta_{23}=0.388-0.665\sqrt{\frac{E_m}{E_f}}+2.56\frac{E_m}{E_f} \quad \text{A.2.7}$$

$$v_{23} = k(v_f V_f + v_m V_m) \quad \text{A.2.8}$$

$$k=1.095+0.27(0.8-V_f) \quad \text{A.2.9}$$

### A.3 Analytical Homogenization Method

The lamina's engineering constants could be explicitly obtained in terms of the coefficients of the stiffness tensor [17,45].

$$E_1 = C_{11}^* - \frac{2C_{12}^{*2}}{C_{22}^* + C_{33}^*} \quad \text{A.3.1}$$

$$E_2 = \frac{(2C_{11}^*C_{22}^* + 2C_{11}^*C_{23}^* - 4C_{12}^{*2})(C_{22}^* - C_{23}^* + 2C_{44}^*)}{3C_{11}^*C_{22}^* + C_{11}^*C_{23}^* + 2C_{11}^*C_{44}^* - 4C_{12}^{*2}} \quad \text{A.3.2}$$

$$G_{12} = G_{13} = C_{66}^* \quad \text{A.3.3}$$

$$v_{12} = v_{13} = \frac{C_{12}^*}{C_{22}^* + C_{23}^*} \quad \text{A.3.4}$$

$$v_{23} = \frac{C_{11}^*C_{22}^* + 3C_{11}^*C_{23}^* - 2C_{11}^*C_{44}^* - 4C_{12}^{*2}}{3C_{11}^*C_{22}^* + C_{11}^*C_{23}^* + 2C_{11}^*C_{44}^* - 4C_{12}^{*2}} \quad \text{A.3.5}$$

$$G_{23} = \frac{C_{22}^*}{4} - \frac{C_{23}^*}{4} + \frac{C_{44}^*}{2} = \frac{E_2}{2(1+v_{23})} \quad \text{A.3.6}$$

where:  $C_{ij}^*$  ( $i=1\dots3, j=1\dots3$ ) is coefficients of the stiffness tensor. It is assumed that the composite has periodic microstructure in a square array, and that the Fourier series could be used to estimate all the components of stiffness tensor. In terms of square symmetrical microstructure, the stiffness tensor has six unique coefficients [17] given as follows:

$$C_{11}^* = \lambda_m + 2\mu_m - \frac{V_f}{D} \left[ \frac{S_3^2}{\mu_m^2} - \frac{2S_6S_3}{\mu_m^2 g} - \frac{aS_3}{\mu_m c} + \frac{S_6^2 - S_7^2}{\mu_m^2 g^2} + \frac{aS_6 + bS_7}{\mu_m gc} + \frac{a^2 - b^2}{4c^2} \right] \quad \text{A.3.7}$$

$$C_{12}^* = \lambda_m + \frac{bV_f}{D} \left[ \frac{S_3}{2c\mu_m} - \frac{S_6 - S_7}{2c\mu_m g} - \frac{a + b}{4c^2} \right] \quad \text{A.3.8}$$

$$C_{23}^* = \lambda_m + \frac{V_f}{D} \left[ \frac{aS_7}{2\mu_m gc} - \frac{ba + b^2}{4c^2} \right] \quad \text{A.3.9}$$

$$C_{22}^* = \lambda_m + 2\mu_m - \frac{V_f}{D} \left[ -\frac{aS_3}{2\mu_m c} + \frac{aS_6}{2\mu_m gc} + \frac{a^2 - b^2}{4c^2} \right] \quad \text{A.3.10}$$

$$C_{44}^* = \mu_m - V_f \left[ -\frac{2S_3}{\mu_m} + (\mu_m - \mu_f)^{-1} + \frac{4S_7}{\mu_m (2-2\nu_m)} \right]^{-1} \quad \text{A.3.11}$$

$$C_{66}^* = \mu_m - V_f \left[ -\frac{S_3}{\mu_m} + (\mu_m - \mu_f)^{-1} \right]^{-1} \quad \text{A.3.12}$$

where:

$$D = \frac{aS_3^2}{2\mu_m^2 c} - \frac{aS_3 S_6}{\mu_m^2 gc} + \frac{a(S_6^2 - S_7^2)}{2\mu_m^2 g^2 c} + \frac{S_3(b^2 - a^2)}{2\mu_m c^2} + \frac{S_6(a^2 - b^2) + S_7(ab + b^2)}{2\mu_m gc^2} + \frac{(a^3 - 2b^3 - 3a)}{8c^3} \quad \text{A.3.13}$$

$$a = \mu_f - \mu_m - 2\mu_f \nu_m + 2\mu_m \nu_f \quad \text{A.3.14}$$

$$b = -\mu_m \nu_m + \mu_f \nu_f + 2\mu_m \nu_m \nu_f - 2\mu_f \nu_m \nu_f \quad \text{A.3.15}$$

$$c = (\mu_m - \mu_f)(\mu_f - \mu_m + \mu_f \nu_f - \mu_m \nu_m + 2\mu_m \nu_f - 2\mu_f \nu_m + 2\mu_m \nu_m \nu_f - 2\mu_f \nu_m \nu_f) \quad \text{A.3.16}$$

$$g = 2 - 2\nu_m \quad \text{A.3.17}$$

$$S_3 = 0.49247 - 0.47603V_f - 0.02748V_f^2 \quad \text{A.3.18}$$

$$S_6 = 0.36844 - 0.14944V_f - 0.271582V_f^2 \quad \text{A.3.19}$$

$$S_7 = 0.12364 - 0.32035V_f - 0.23517V_f^2 \quad \text{A.3.20}$$

$$\lambda = \frac{E}{(1+\nu)(1-2\nu)} \quad \text{A.3.21}$$

$$\mu = G \quad \text{A.3.22}$$

## APPENDIX B: Prediction of Ultimate Strength

**B.1 Ultimate Longitudinal Tensile Strength:** By assuming that all the fibers have the same tensile strength, both the fibers and the matrix behave linearly up to failure, the fibers are brittle with respect to the matrix and the fibers are stiffer than the matrix, the longitudinal tensile strength is controlled by the fiber strength and represented as follows based on roles of mixtures. [15,18,19]

$$F_{lt} = F_{ft} \left( V_f + \frac{E_m}{E_f} V_m \right) \quad \text{B.1.1}$$

where:  $F_{ft}$  is the fiber tensile strength.

## B.2 Ultimate Longitudinal Compressive Strength

**B.2.1 Roles of Mixtures:** Based on assumption of *roles of mixtures*, the longitudinal compressive strength could simply be predicted as the smaller value obtained from Eqn. B.2.1 [15].

$$F_{lc} = \begin{cases} F_{fc} \left[ \beta V_f + V_m \frac{E_m}{E_f} \right] \\ F_{mc} \left[ V_m + \beta V_f \frac{E_m}{E_f} \right] \end{cases} \quad \text{B.2.1}$$

where:  $\beta$  is a correction coefficient for longitudinal compressive strength,  $F_{fc}$  is the compressive strength of fibers,  $F_{mc}$  is the matrix compressive strength..

**B.2.2 Fiber Buckling Method:** The longitudinal compressive failure mode is assumed to be triggered by fiber micro-buckling when individual fibers buckle within the matrix. In this case, the longitudinal compressive strength is considered to be the smaller value of in-phase shear mode and out-of-phase mode [15, 18].

$$F_{lc} = \begin{cases} 2V_f \sqrt{\frac{\beta E_f E_m V_f}{3V_m}} & \text{In - phase shear mode} \\ \frac{\beta G_m}{1 - V_f} & \text{out - of - phase mode} \end{cases} \quad \text{B.2.2}$$

**B.2.3 Improved Fiber Buckling Method:** The fiber buckling method is improved to account for fiber misalignment and expressed as follows [15]:

$$F_{1c} = G_{12} \left(1 + \frac{4.76 G_{12} \alpha_{\sigma}}{S}\right)^{-0.69} \quad \text{B.2.3}$$

where:  $\alpha_{\sigma}$  is the standard deviation of fiber misalignment which could be measured experimentally.

### B.3 Ultimate Transverse Tensile Strength

**B.3.1 Strength Concentration Method:** It is assumed that the transverse strength of composites is controlled by the matrix ultimate strength and is lower than the matrix strength by a factor known as strength concentration factor (*SCF*), which depended on the relative properties of the fibers and the matrix and their volume fractions. Thus, the transverse composite strength could be expressed as [18]:

$$F_{2t} = F_{mt} / SCF \quad \text{B.3.1}$$

where:  $F_{mt}$  is the matrix tensile strength. Agarwal et al. [18] proposed the following expression for determining *SCF*:

$$SCF = \frac{1 - V_f [1 - E_m / E_f]}{1 - (4V_f / \pi)^{1/2} [1 - E_m / E_f]} \quad \text{B.3.2}$$

Huang [20] also proposed *SCF* formula with transversely isotropic fibers derived upon isotropic fiber reinforcement as:

$$SCF = \left[ 1 + \frac{\sqrt{V_f}}{2} A' + \frac{\sqrt{V_f}}{2} (3 - V_f - \sqrt{V_f}) B' \right] \left[ \frac{(V_f + \beta V_m) E_{f2} + V_m (1 - \beta) E_m}{\beta E_{f2} + (1 - \beta) E_m} \right] \quad \text{B.3.3}$$

$$A' = \frac{[1 - \nu_m - 2\nu_m^2] E_{f2} - [1 - \nu_{f23} - 2\nu_{f23}^2] E_m}{E_{f2} (1 + \nu_m) + E_m (1 - \nu_{f23} - 2\nu_{f23}^2)} \quad \text{B.3.4}$$

$$B' = \frac{E_m (1 + \nu_{f23}) - E_{f2} (1 + \nu_m)}{E_{f2} (-3 + \nu_m + 4\nu_m^2) - E_m (1 + \nu_{f23})} \quad \text{B.3.5}$$

where:  $\beta$  is bridging parameter.

**B.3.2 Fracture Mechanic Method:** It is assumed that the transverse tensile failure of a



unidirectional lamina occurs when a transverse crack propagates along the fiber direction [15], the transverse tensile strength could be obtained as follows:

$$F_{2t} = \sqrt{\frac{G_{Ic}}{1.12^2 \pi (t_t / 4) \Lambda_{22}^0}} \quad \text{B.3.6}$$

$$\Lambda_{22}^0 = 2 \left( \frac{1}{E_2} - \frac{v_{12}^2 E_2^2}{E_1^3} \right) \quad \text{B.3.7}$$

where:  $G_{Ic}$  is the fracture toughness in mode I,  $t_t$  is the transition thickness and could be approximated as 0.6 mm for E-glass-epoxy composites.

**B.3.3 Empirical Formula:** An empirical formula for estimating the transverse tensile strength is adopted [15, 23, 24].

$$F_{2t} = F_{mt} \left[ 1 - \sqrt{\frac{4V_v}{\pi(1-V_f)}} \right] \left[ 1 + (V_f - \sqrt{V_f}) \left( 1 - \frac{E_m}{E_{f2}} \right) \right] \quad \text{B.3.8}$$

where:  $V_v$  is the void volume fraction,  $F_{mt}$  is the matrix tensile strength.

## B.4 Ultimate Transverse Compressive Strength

**B.4.1 Strain Amplification Method:** The transverse compressive strength could be obtained by strain-amplification factor method as follows [21, 22]:

$$F_{2c} = E_2 \varepsilon_{mc} \left\{ 1 - (4V_f / \pi)^{1/2} [1 - E_m / E_f] \right\} \quad \text{B.4.1}$$

where:  $\varepsilon_{mc}$  is the matrix ultimate compressive strain.

**B.4.2 Strain Amplification Method:** An empirical formula for estimating the transverse compressive strength is given by [15, 23, and 24]:

$$F_{2c} = F_{mc} \left[ 1 - \sqrt{\frac{4V_v}{\pi(1-V_f)}} \right] \left[ 1 + (V_f - \sqrt{V_f}) \left( 1 - \frac{E_m}{E_{f2}} \right) \right] \quad \text{B.4.2}$$

## B.5 Ultimate In-Plane Shear Strength

**B.5.1 Roles of Mixtures:** It assumed that in-plane shear failure occurs when a transverse crack propagates [15].

$$S = \sqrt{\frac{G_{2c} G_{12}}{\pi(t_t / 4)}} \quad \text{B.5.1}$$

where:  $G_{2c}$  is the fracture toughness in mode II.

**B.5.2 Fracture Mechanic Method:** Similar to transverse compressive strength, one empirical formulas is also adopted. [15, 23, 24]

$$S = S_m \left[ 1 - \sqrt{\frac{4V_v}{\pi(1-V_f)}} \right] \left[ 1 + (V_f - \sqrt{V_f}) \left( 1 - \frac{G_m}{G_f} \right) \right] \quad \text{B.5.2}$$

## REFERENCES

- [1] Mosallam AS, Bayraktar A, Elmikawi M, Pul S, Adanur S. Polymer composites in construction: an overview. SOJ Mat. Sci. Eng., Open Access, 2015.
- [2] Bank LC. Composites for construction: structural design with FRP materials. John Wiley & Sons; 2006.
- [3] Xin H, Liu Y, He J, Fan H, Zhang Y. Fatigue behavior of hybrid GFRP-concrete bridge decks under sagging moment. Steel Compos. Struct., 2015; 18:925–46.
- [4] Xin H, Liu Y, Du A. Thermal analysis on composite girder with hybrid GFRP-concrete deck. Steel Compos Struct 2015; 19:1221–36.
- [5] Ascione L, Caron J-F, Godonou P, van IJselmuiden K, Knippers J, Mottram T, et al. Prospect for new guidance in the design of FRP: Support to the implementation, harmonization and further development of the Eurocodes. Publications Office of the European Union; 2016.

- [6] Xin H, Liu Y, Mosallam A, Zhang Y, Wang C. Hygrothermal aging effects on flexural behavior of pultruded glass fiber reinforced polymer laminates in bridge applications. *Constr. Build Mater* 2016; 127:237–47.
- [7] Xin H, Liu Y, Mosallam A, Zhang Y. Moisture diffusion and hygrothermal aging of pultruded glass fiber reinforced polymer laminates in bridge application. *Compos Part B Eng* 2016; 100:197–207.
- [8] Xin H, Mosallam A, Liu Y, Wang C, Zhang Y. Impact of hygrothermal aging on rotational behavior of web-flange junctions of structural pultruded composite members for bridge applications. *Compos Part B Eng* 2017; 110:279–97.
- [9] Xin H, Mosallam A, Liu Y, Yang F, Zhang Y. Hygrothermal aging effects on shear behavior of pultruded FRP composite web-flange junctions in bridge application. *Compos Part B Eng* 2017; 110:213–28. doi:10.1016/j.compositesb.2016.10.093.
- [10] Schniepp TJ. Design manual development for a hybrid, FRP double-web beam and characterization of shear stiffness in FRP composite beams 2002.
- [11] He J, Liu Y, Chen A, Dai L. Experimental investigation of movable hybrid GFRP and concrete bridge deck. *Constr. Build Mater* 2012; 26:49–64.
- [12] Xin H, Mosallam A, Liu Y, Wang C, Zhang Y. Analytical and experimental evaluation of flexural behavior of FRP pultruded composite profiles for bridge deck structural design. *Constr. Build Mater* 2017; 150:123–49.
- [13] Xin H, Mosallam A, Liu Y, Xiao Y, He J, Wang C, et al. Experimental and Numerical Investigation on In-Plane Compression and Shear Performance of a Pultruded GFRP Composite Bridge Deck. *Compos Struct* 2017:914–32.
- [14] Xin H, Liu Y, Mosallam AS, He J, Du A. Evaluation on material behaviors of pultruded

- glass fiber reinforced polymer (GFRP) laminates. *Compos Struct* 2017.
- [15] Barbero EJ. *Introduction to composite materials design*. CRC press; 2010.
- [16] Hahn HT, Tsai SW. *Introduction to composite materials*. CRC Press; 1980.
- [17] Barbero EJ. *Finite element analysis of composite materials using Abaqus™*. CRC press; 2013.
- [18] Agarwal BD, Broutman LJ, Chandrashekhara K. *Analysis and performance of fiber composites*. John Wiley & Sons; 2006.
- [19] Jones RM. *Mechanics of composite materials*. vol. 193. Scripta Book Company Washington, DC; 1975.
- [20] Liu L, Huang Z-M. Stress concentration factor in matrix of a composite reinforced with transversely isotropic fibers. *J Compos Mater* 2014; 48:81–98.
- [21] Davydenko VI. Strength and deformability of reinforced polymers in tension normal to the fibers. *Mech Compos Mater* 1970; 6:595–9.
- [22] Schulz J. Maximum stresses and strains in the resin of a filament-wound structure, 1963.
- [23] Weeton JW, Thomas KL, Peters DM. *Engineers' guide to composite materials*. American Society of Metals; 1987.
- [24] Stellbrink KK. *Micromechanics of composites: composite properties of fibre and matrix constituents*. vol. 1. Hanser Gardner Pubns; 1996.
- [25] González C, LLorca J. Mechanical behavior of unidirectional fiber-reinforced polymers under transverse compression: microscopic mechanisms and modeling. *Compos Sci Technol*. 2007; 67:2795–806.
- [26] Fish J. *Practical Multiscale*. John Wiley & Sons; 2013.
- [27] Vaughan TJ, McCarthy CT. *Micromechanical modelling of the transverse damage*

- behaviour in fibre reinforced composites. *Compos. Sci. Technol.* 2011; 71:388–96.
- [28] Soni G, Singh R, Mitra M, Falzon BG. Modelling matrix damage and fibre–matrix interfacial decohesion in composite laminates via a multi-fibre multi-layer representative volume element (M<sup>2</sup> RVE). *Int. J. Solids Struct*, 2014; 51:449–61.
- [29] Romanowicz M. A numerical approach for predicting the failure locus of fiber reinforced composites under combined transverse compression and axial tension. *Comput. Mat. Sci.* 2012; 51:7–12.
- [30] Melro AR, Camanho PP, Pires FMA, Pinho ST. Micromechanical analysis of polymer composites reinforced by unidirectional fibres: Part I – Constitutive modelling. *Int J Solids Struct* 2013; 50:1897–905.
- [31] Melro AR, Camanho PP, Pires FMA, Pinho ST. Micromechanical analysis of polymer composites reinforced by unidirectional fibres: Part II – Micromechanical analyses. *Int J Solids Struct* 2013; 50:1906–15.
- [32] Ullah Z, Kaczmarczyk L, Pearce CJ. Three-dimensional nonlinear micro/meso-mechanical response of the fibre-reinforced polymer composites. *Compos Struct* 2017; 161:204–14.
- [33] Fish J, Fan R. Mathematical homogenization of nonperiodic heterogeneous media subjected to large deformation transient loading. *Int. J. Num. Methods Eng.*, 2008; 76:1044–64.
- [34] ABAQUS V. 6.14 Documentation. Dassault Syst. Simulia Corp., 2014.
- [35] Menetrey P, Willam KJ. Triaxial failure criterion for concrete and its generalization. *ACI Struct J* 1995; 92:311–8.
- [36] Benzeggagh ML, Kenane M. Measurement of mixed-mode delamination fracture

- toughness of unidirectional glass/epoxy composites with mixed-mode bending apparatus. *Compos Sci Technol.* 1996; 56:439–49.
- [37] Soden PD, Hinton MJ, Kaddour AS. Lamina properties, lay-up configurations and loading conditions for a range of fibre-reinforced composite laminates. *Compos Sci Technol.* 1998; 58:1011–22.
- [38] Uddin N. *Developments in fiber-reinforced polymer (FRP) composites for civil engineering.* Elsevier; 2013.
- [39] ISO E. 1172. Text-Glass-Reinf. Plast-Prepregs Mould Compd Laminates-Determ Text-Glass Miner-Fill Content-Calcination Methods ISO 1172 1996 1996.
- [40] ISO E. 1183-1. *Plastics -- Methods Determining Density Non-Cell Plastics -- Part 1 Immers. Method Liquid Pyknometer Method Titration Method,* 2004.
- [41] Standardization Administration of the People's Republic of China (SAPRC GB/T3354-1999). Test method for tensile properties of oriented fiber reinforced plastics, GB/T3354-1999, Beijing, China: SAPRC; 2005(In Chinese) n.d.
- [42] Schneider, K. (2007). Determination of compressive properties of fibre composites in the in-plane direction according to ISO 14126. Part 1: a round Robin test. *Applied Composite Materials*, 14(1), 1-15.
- [43] Standardization Administration of the People's Republic of China (SAPRC GB/T28889-2012). Test method for in-plane shear properties of composites materials, GB/T28889-2012, Beijing, China: SAPRC; 2005(In Chinese)
- [44] Association ACM. Pre-standard for load & resistance factor design (LRFD) of pultruded fiber reinforced polymer (FRP) structures. Arlington, VA, ACMA, 2012
- [45] Aboudi, J. *Mechanics of composite materials: a unified micromechanical approach.* vol.

29, Elsevier; 2013.

## LIST OF FIGURES

**Figure (1):** Pultruded composites vs. laminated composites

**Figure (2):** Typical RVEs of unidirectional FRP composites

**Figure (3):** Illustration of material model

**Figure (4):** Schematic of pultrusion process [38]

**Figure (5):** Tensile specimen (mm)

**Figure (6):** Compressive specimen (mm)

**Figure (7):** In-plane shear specimen (mm)

**Figure (8):** Engineering constants comparison

**Figure (9):** Longitudinal tensile behavior comparison

**Figure (10):** Stress, plastic strain and damage distributions of unit cell under longitudinal tensile loading ( $11$ -direction)

**Figure (11):** Longitudinal compressive behavior comparison

**Figure (12):** Stress, plastic strain and damage distributions of unit cell under longitudinal compressive loading ( $11$ -direction)

**Figure (13):** Transverse tensile behavior comparison

**Figure (14):** Stress, plastic strain and damage distributions of unit cell under transverse tensile loading ( $33$ -direction)

**Figure (15):** Transverse compressive behavior comparison

**Figure (16):** Stress, plastic strain and damage distributions of unit cell under transverse compressive loading ( $33$ -direction)



**Figure (17):** In-plane shear behavior comparison

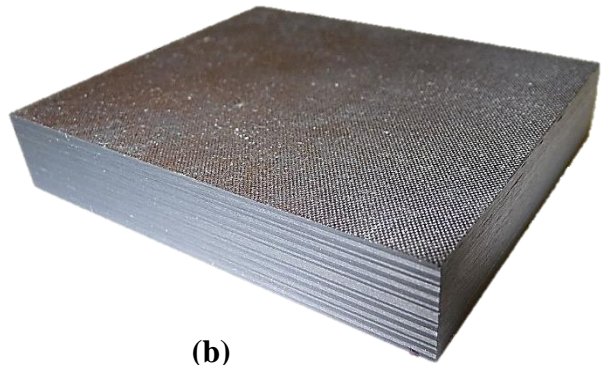
**Figure (18):** Stress, plastic strain and damage distributions of unit cell under in-plane shear loading (*13*-direction)

**Figure (19):** Stress-strain curve of transverse shear

**Figure (20):** Stress, plastic strain and damage distributions of unit cell under transverse shear loading (*23*-direction).



(a)



(b)

**Figure (1):** (a) Pultruded Composites vs. (b) Laminated Composites

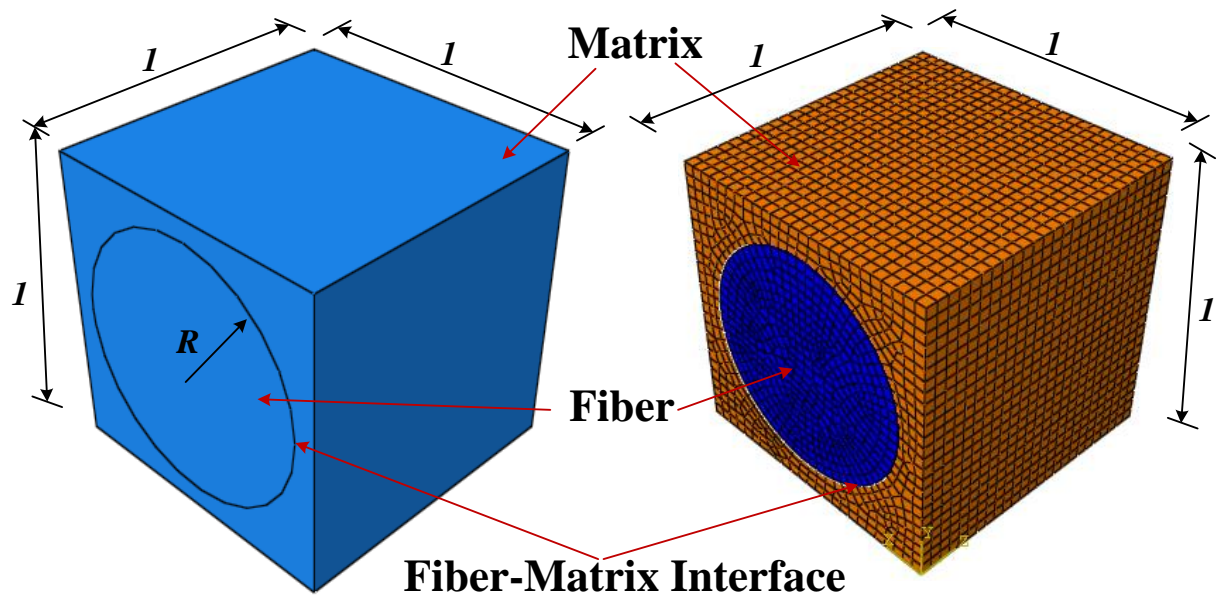


**Figure (2):** Typical RVEs of unidirectional FRP composites

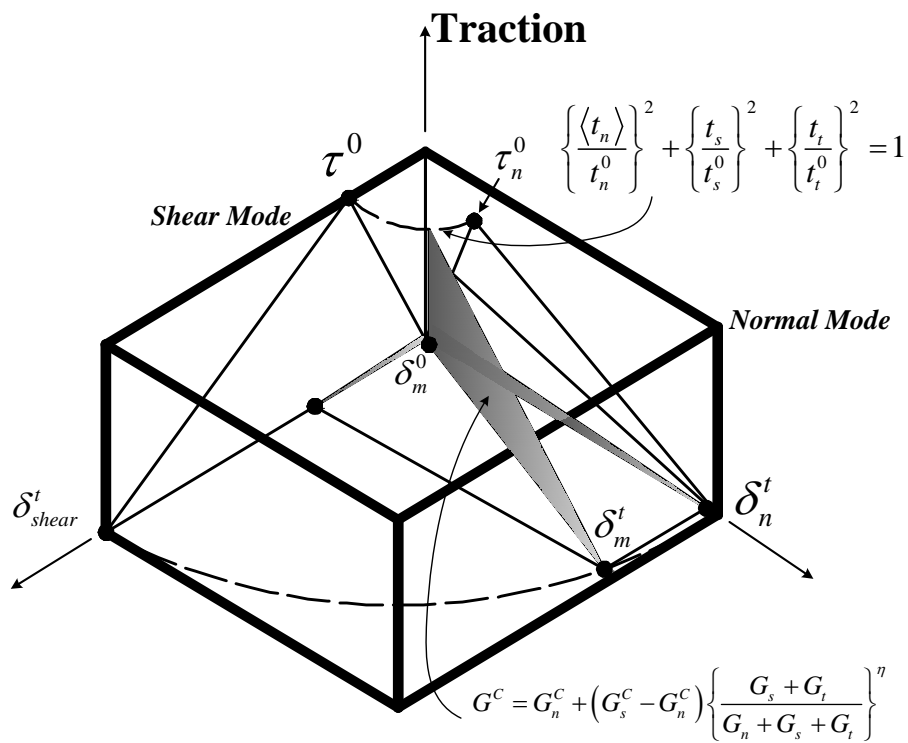
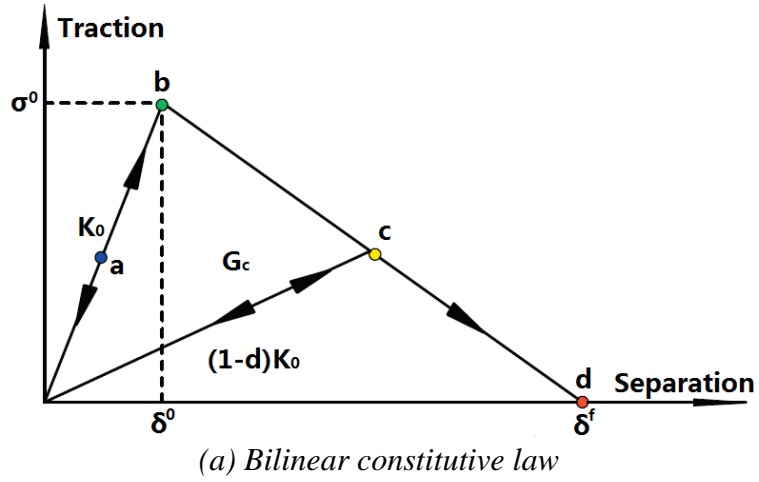


**Figure (3):** Illustration of material model

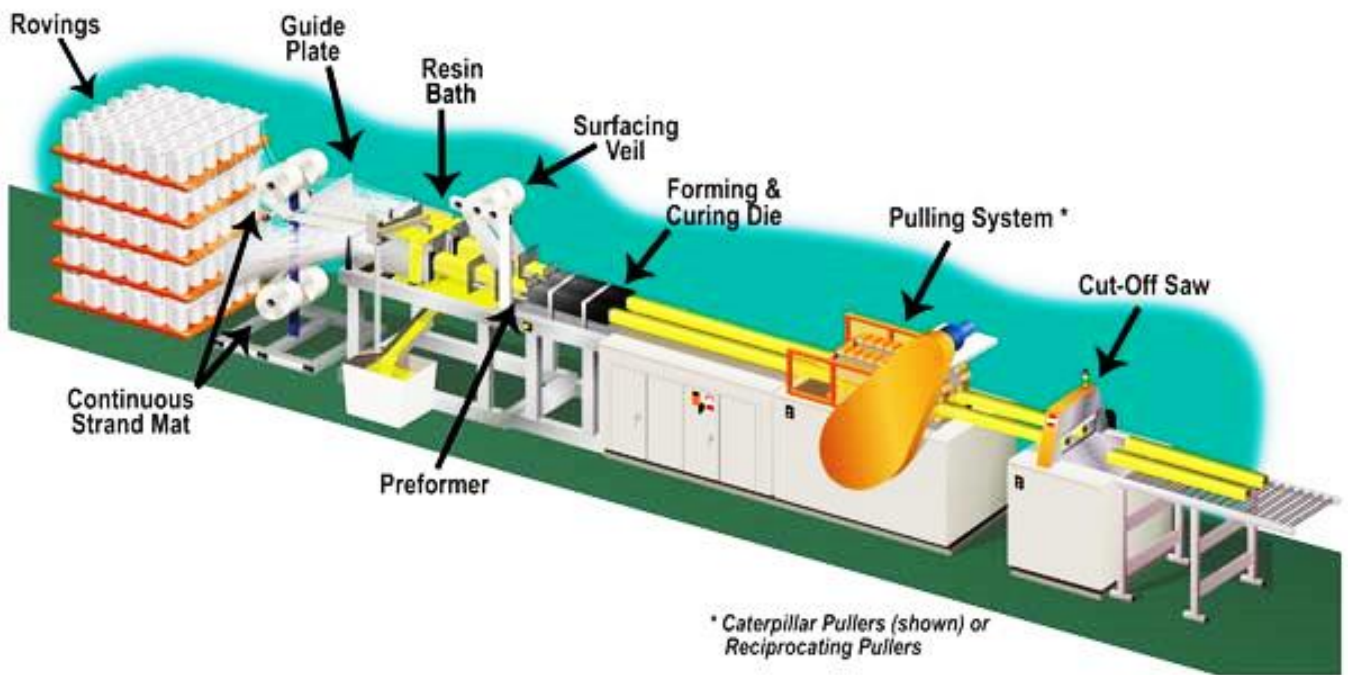
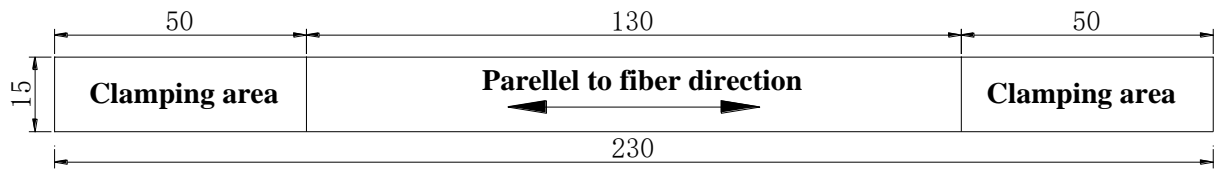
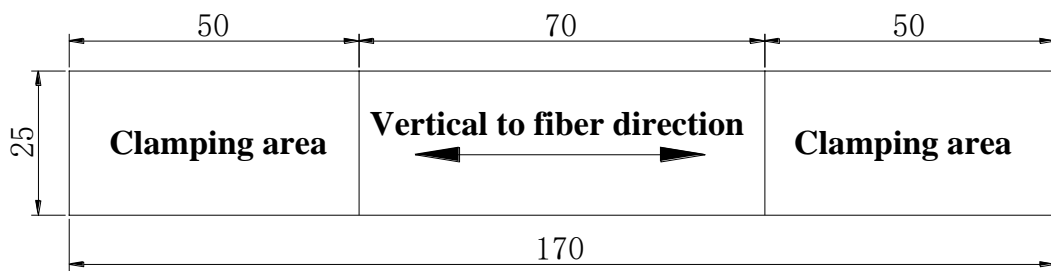


**Figure (4):** Schematic of the pultrusion process [38]

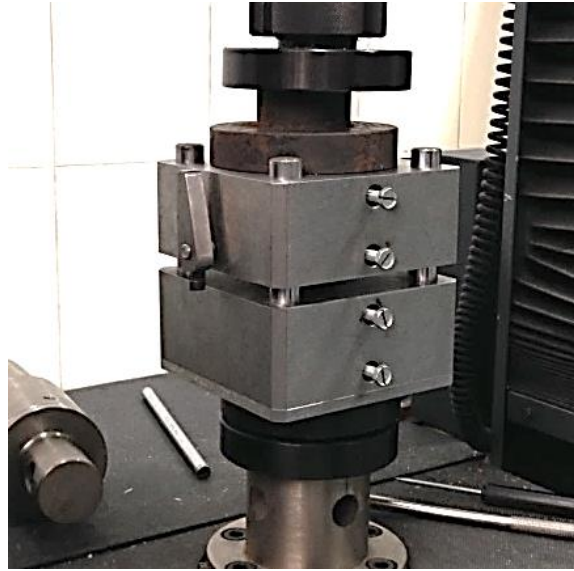


(a) Longitudinal tensile

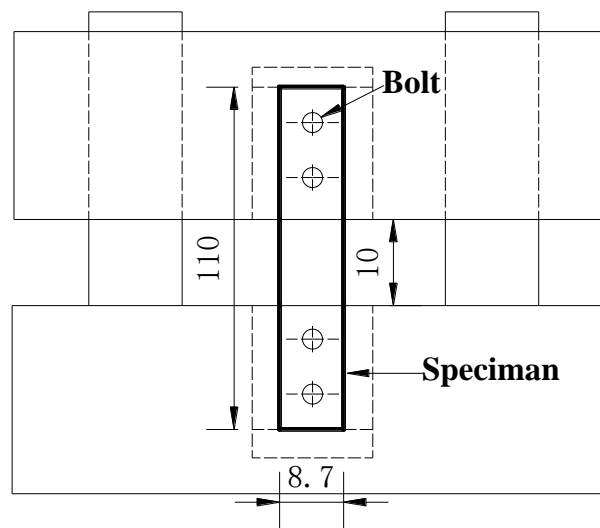


(b) Transverse tensile

**Figure (5):** Dimensions of tensile test specimens (mm)



(a) Set-up Photo



(b) Schematic of experimental set-up

**Figure (6):** Compressive specimen (mm)

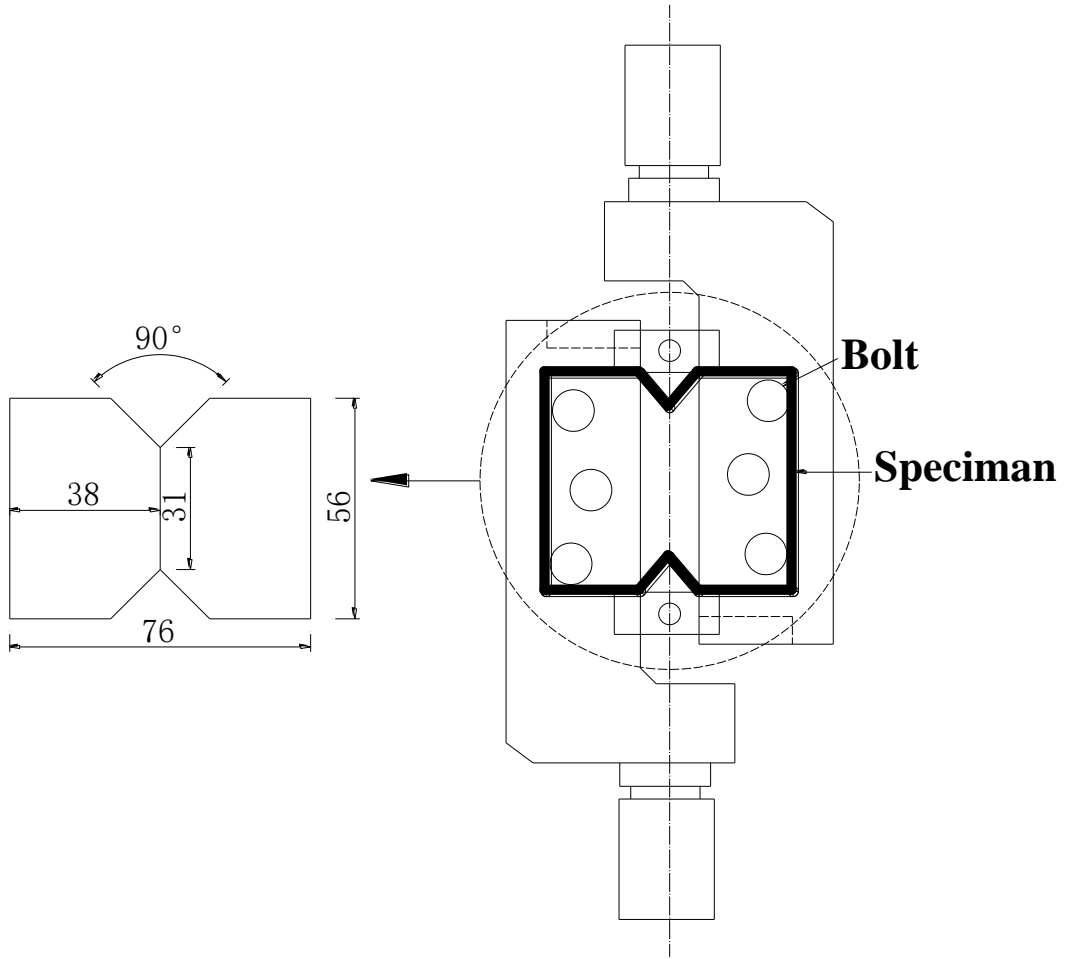
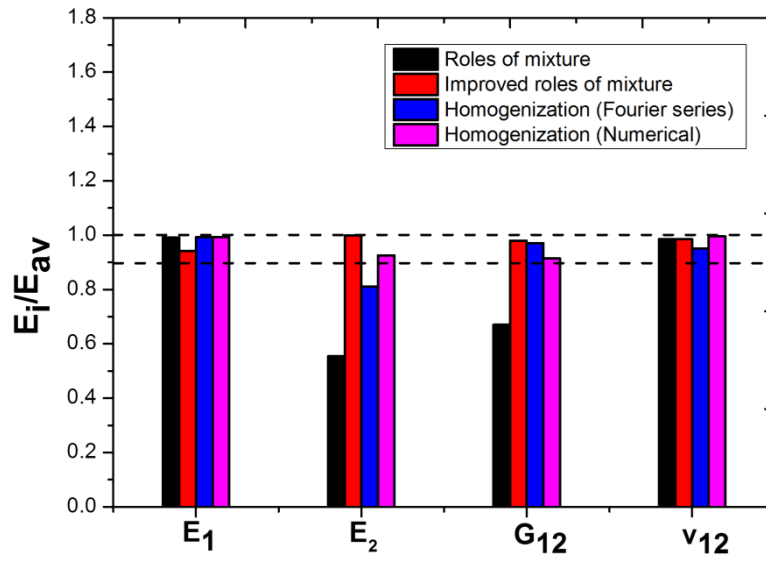
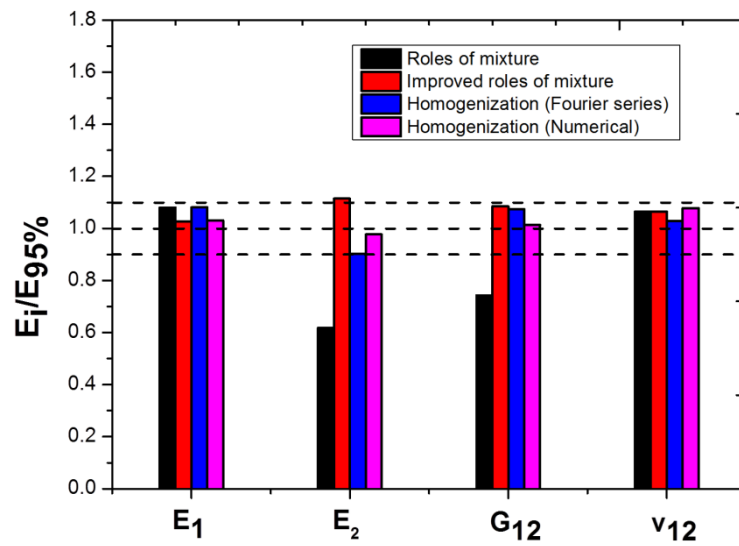


**Figure (7):** In-plane shear specimen (mm)



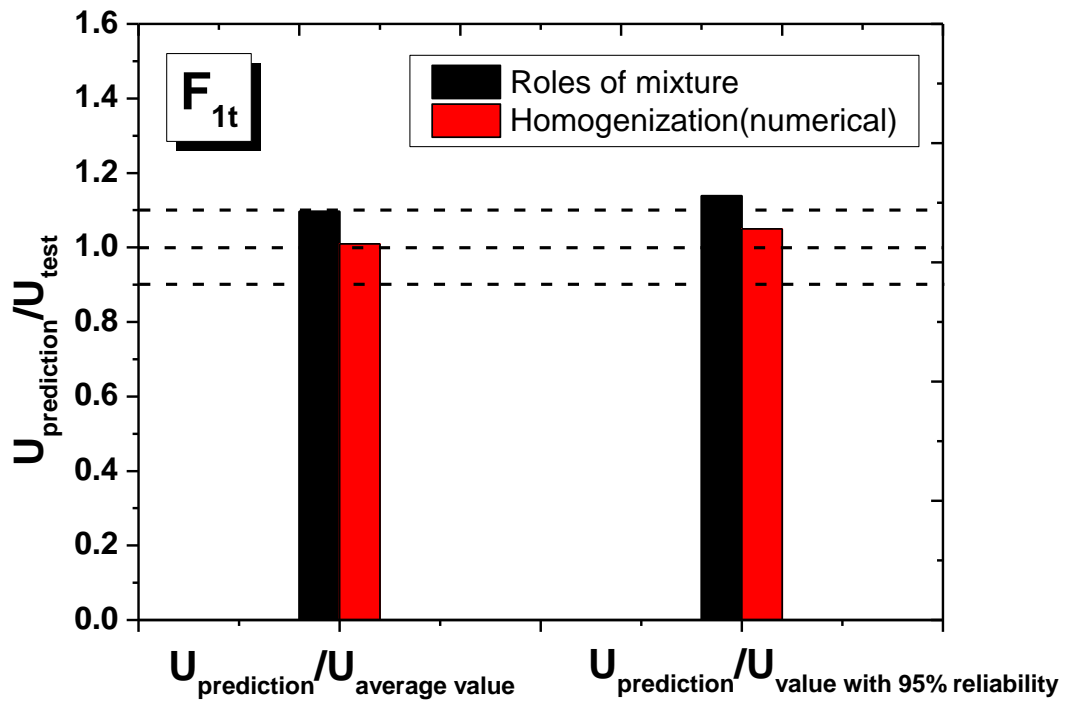


(a) Predicted value to average test results

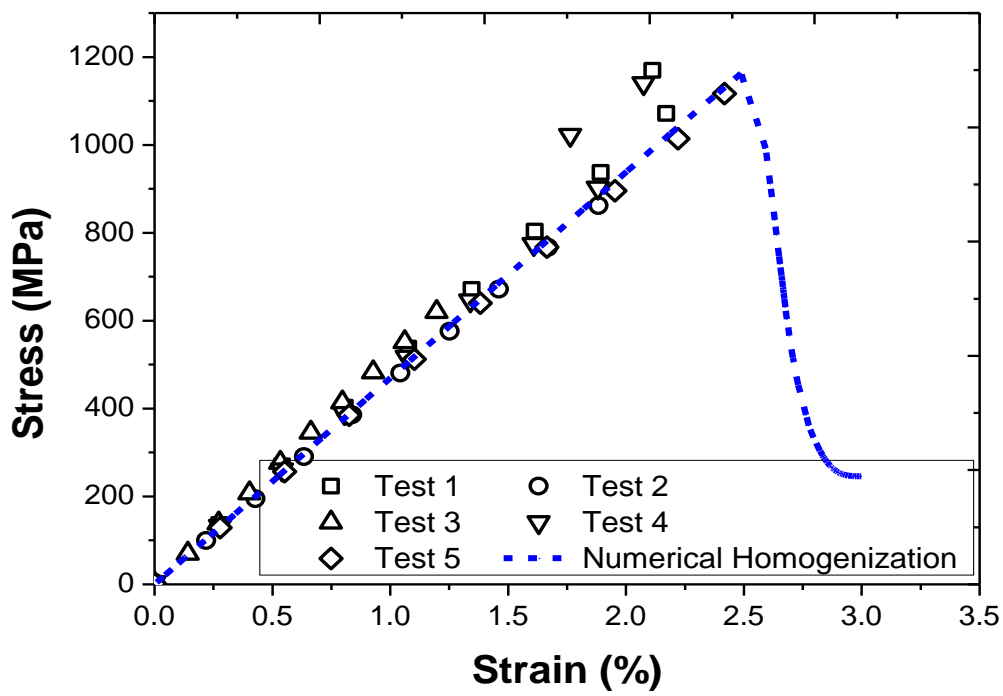


(b) Predicted value to test results with 95% insurance

**Figure (8):** Engineering constants comparison

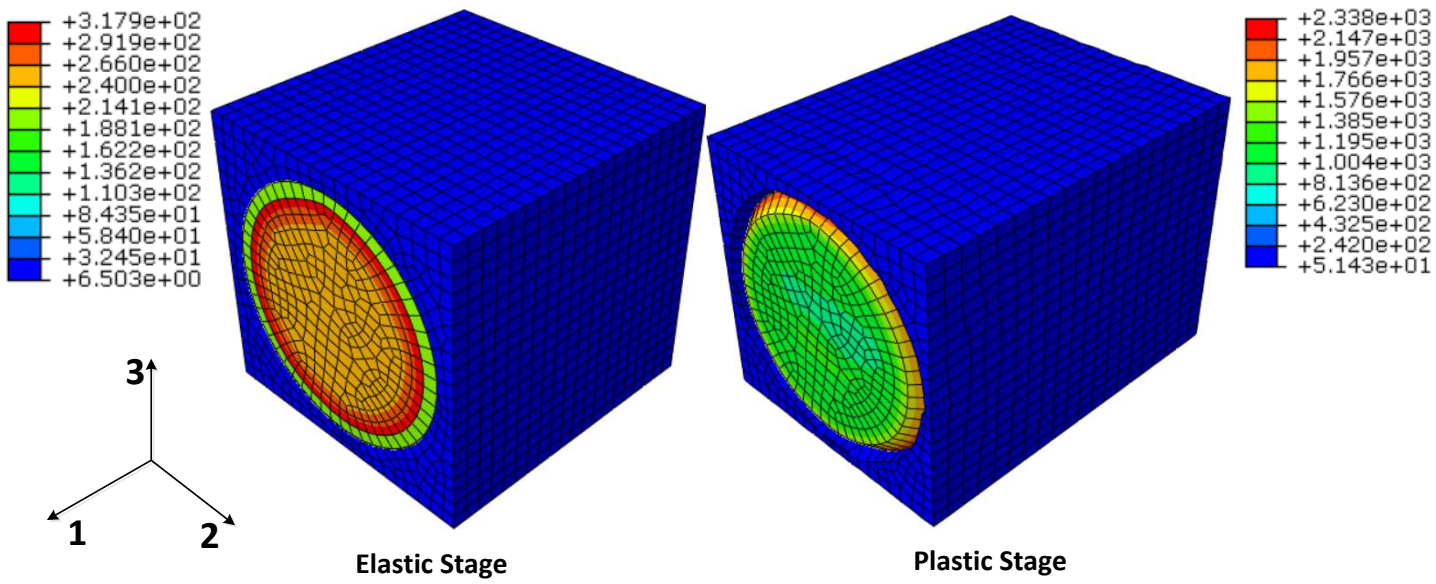


(a) Ultimate strength comparisons

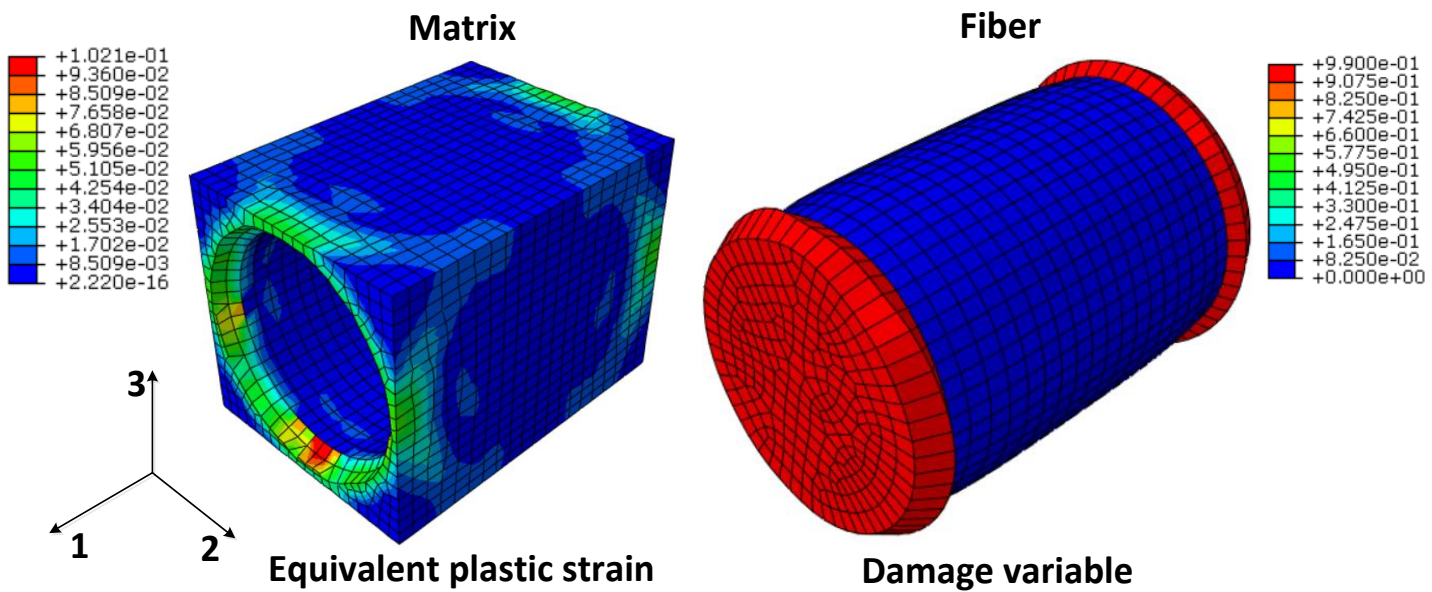


(b) Stress-strain curve comparisons

**Figure (9):** Longitudinal tensile behavior comparison

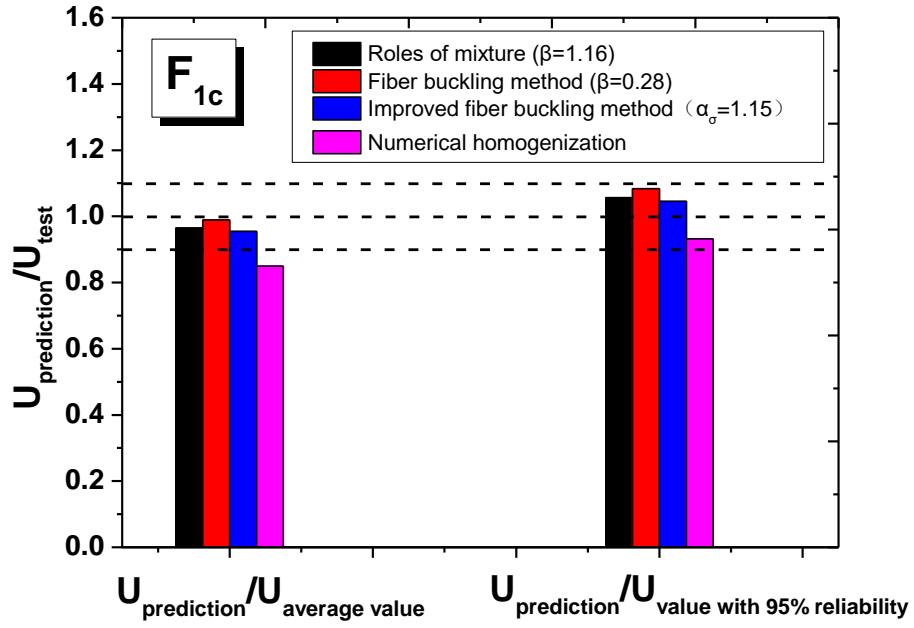


(a) Mises stress

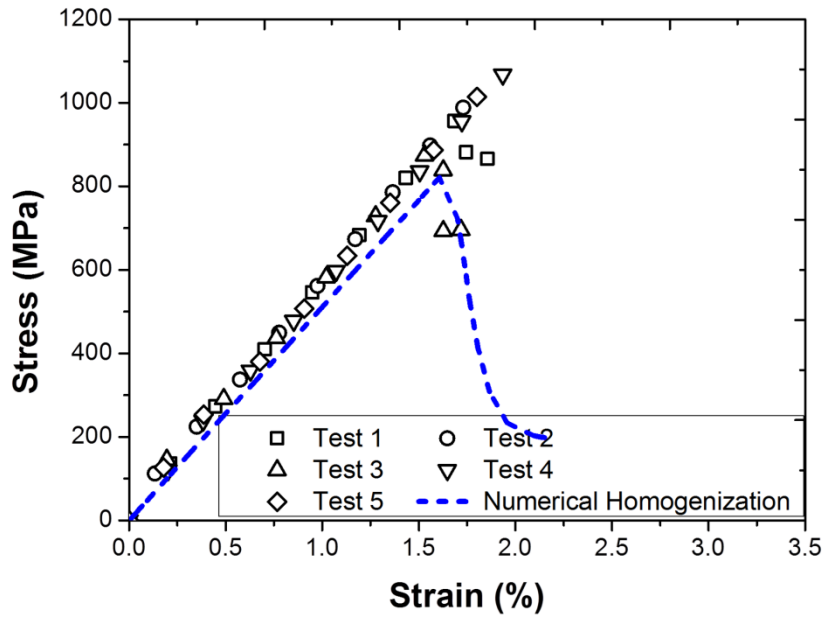


(b) Equivalent plastic strain and damage variable

**Figure (10):** Stress, plastic strain and damage distributions of unit cell under longitudinal tensile loading ( $11$ -direction)

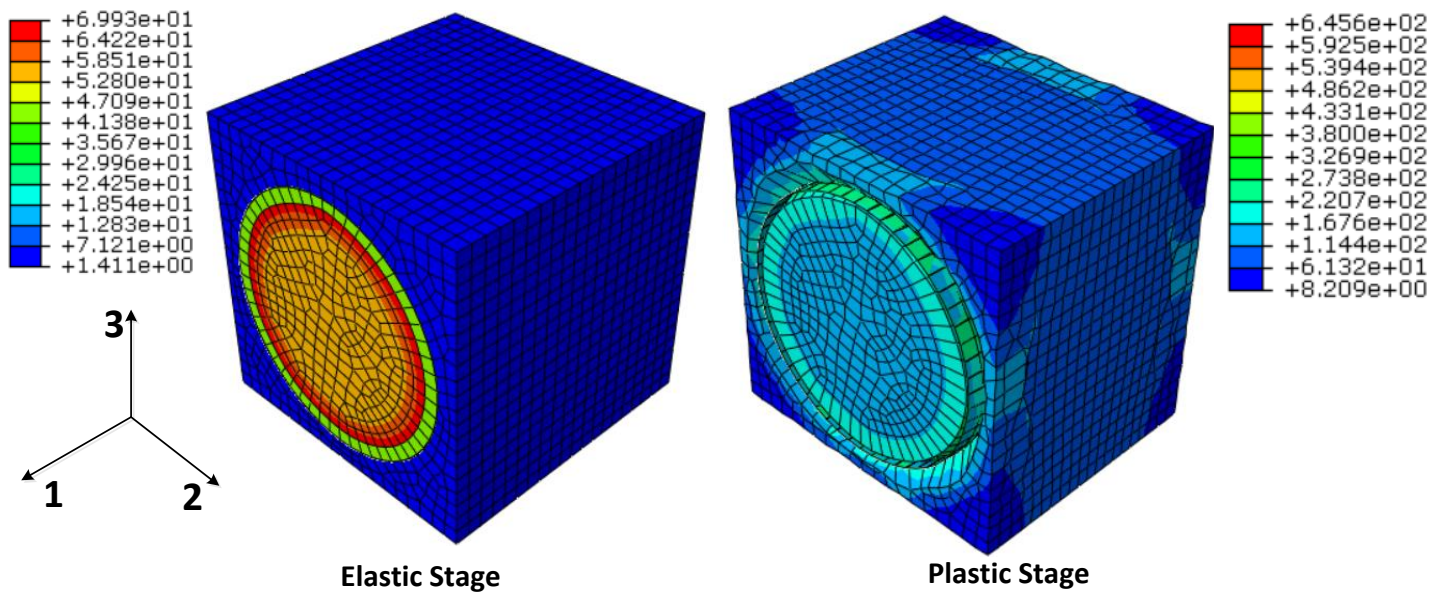


(a) Ultimate strength comparisons

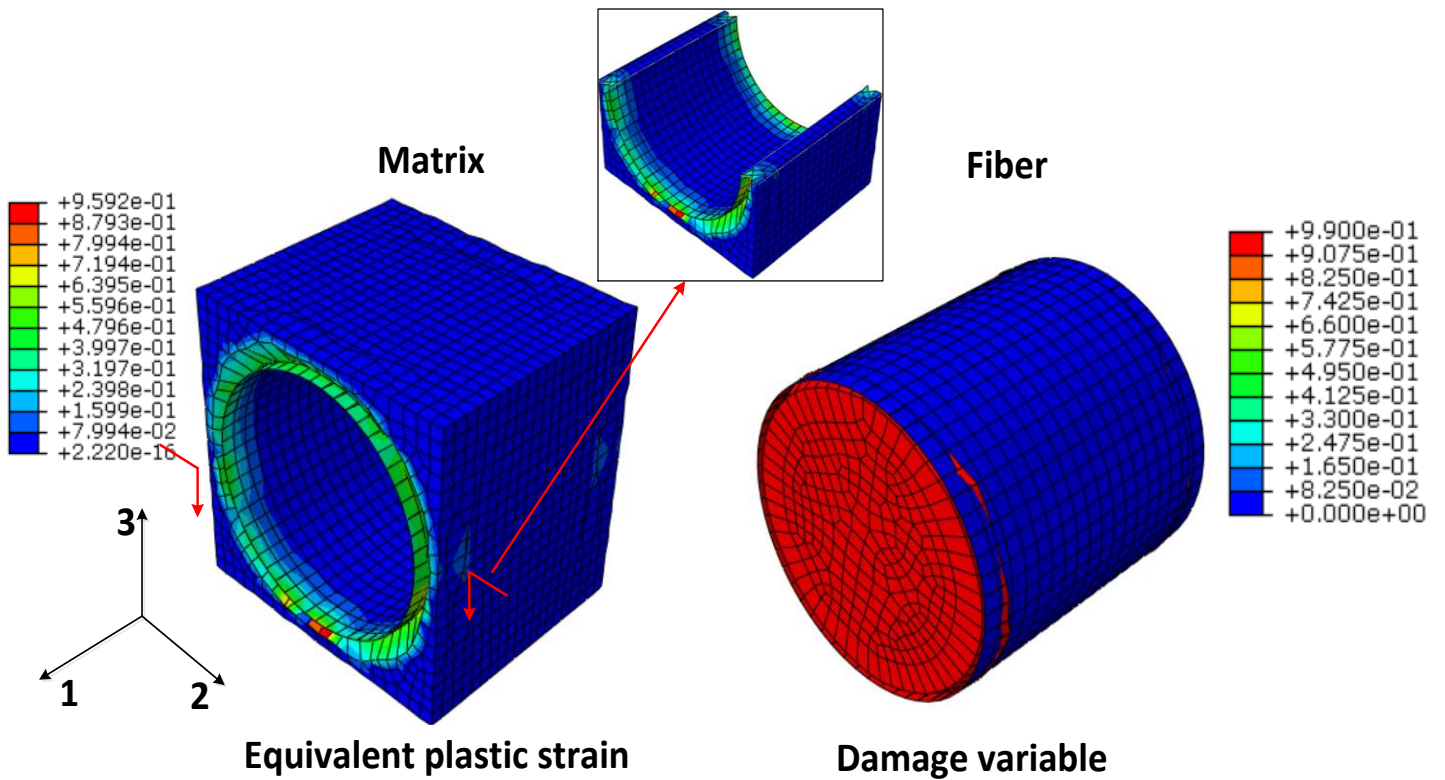


(b) Stress-strain curve comparisons

**Figure (11):** Longitudinal compressive behavior comparison

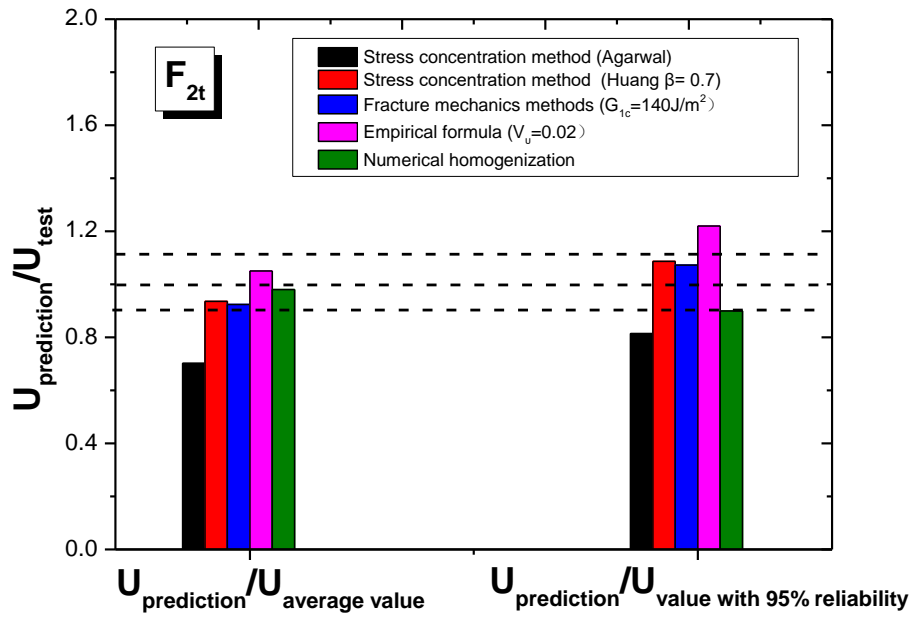


(a) Mises stress

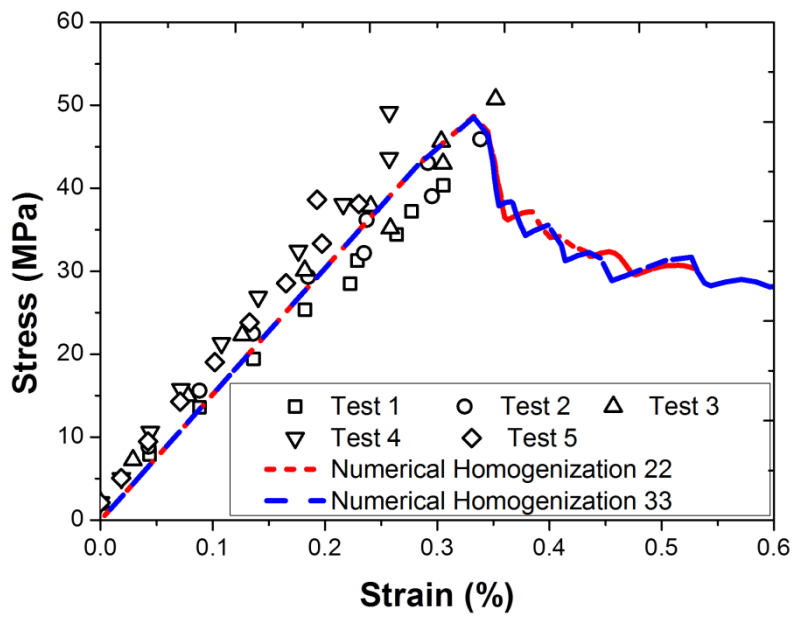


(b) Equivalent plastic strain and damage variable

**Figure (12):** Stress, plastic strain and damage distributions of unit cell under longitudinal compressive loading ( $11$ -direction)

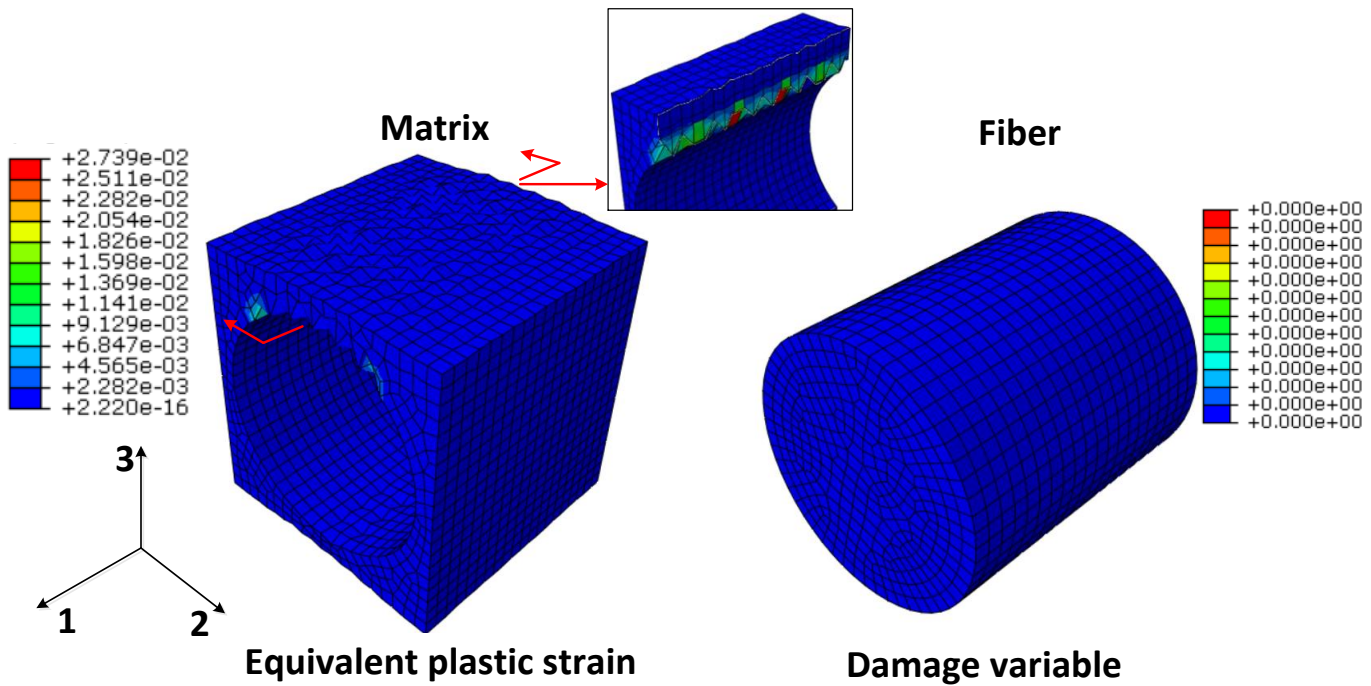
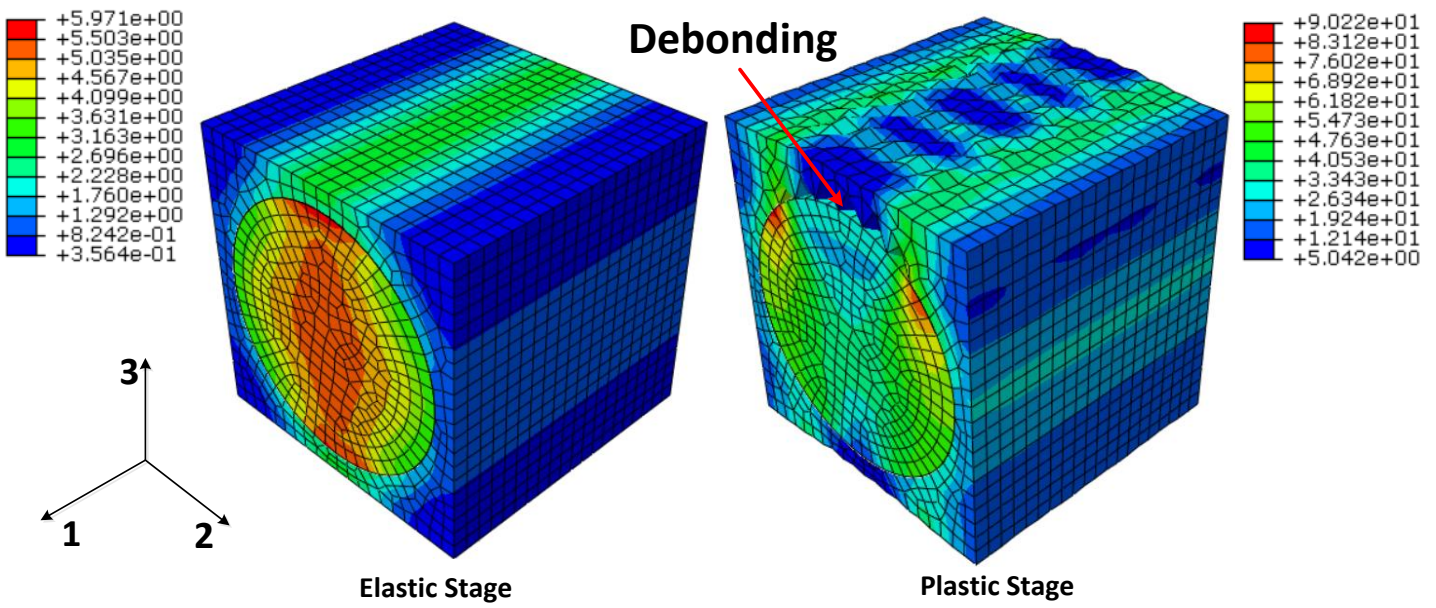


(a) Ultimate strength comparisons

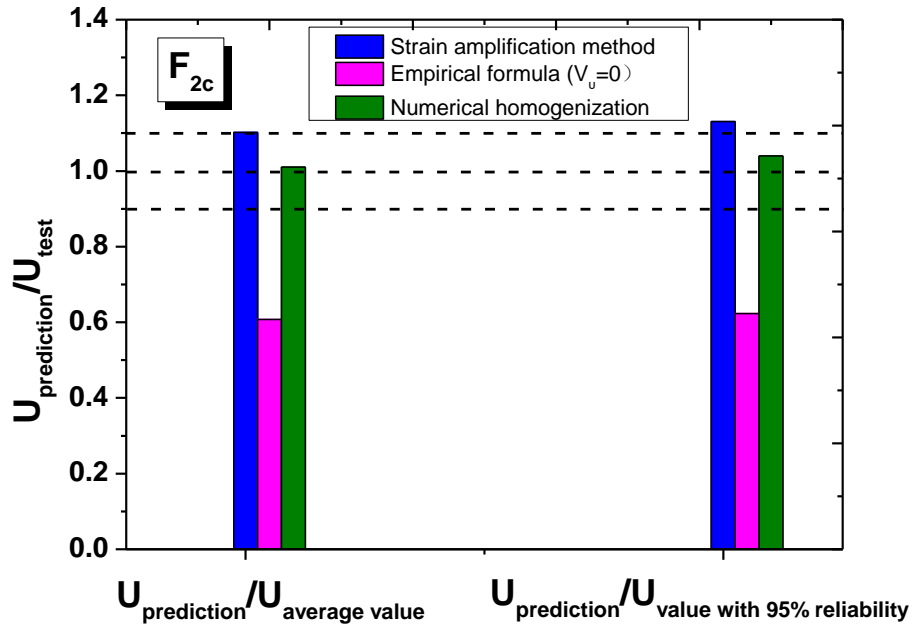


(b) Stress-strain curve comparisons

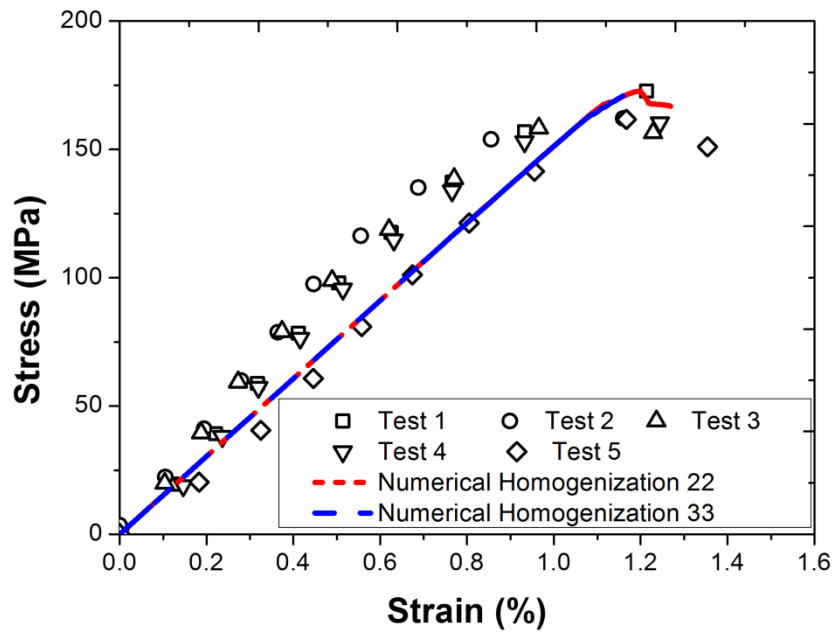
**Figure (13):** Transverse tensile behavior comparison



**Figure (14):** Stress, plastic strain and damage distributions of unit cell under transverse tensile loading (33-direction)



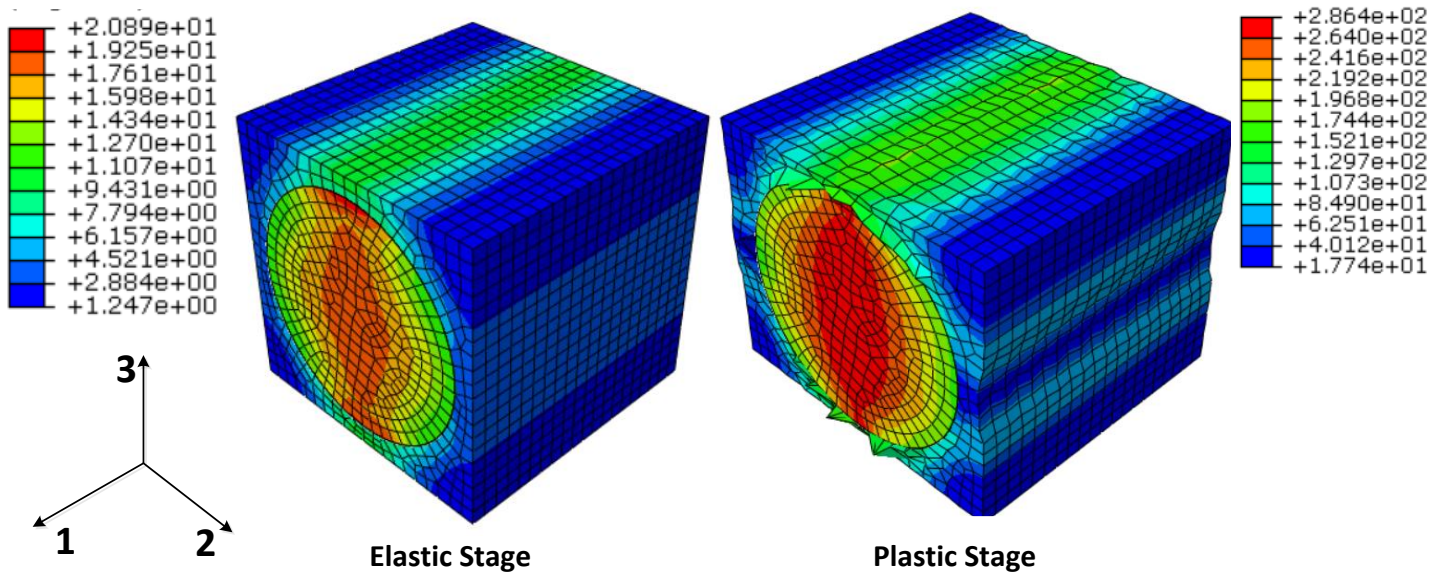
(a) Ultimate strength comparisons



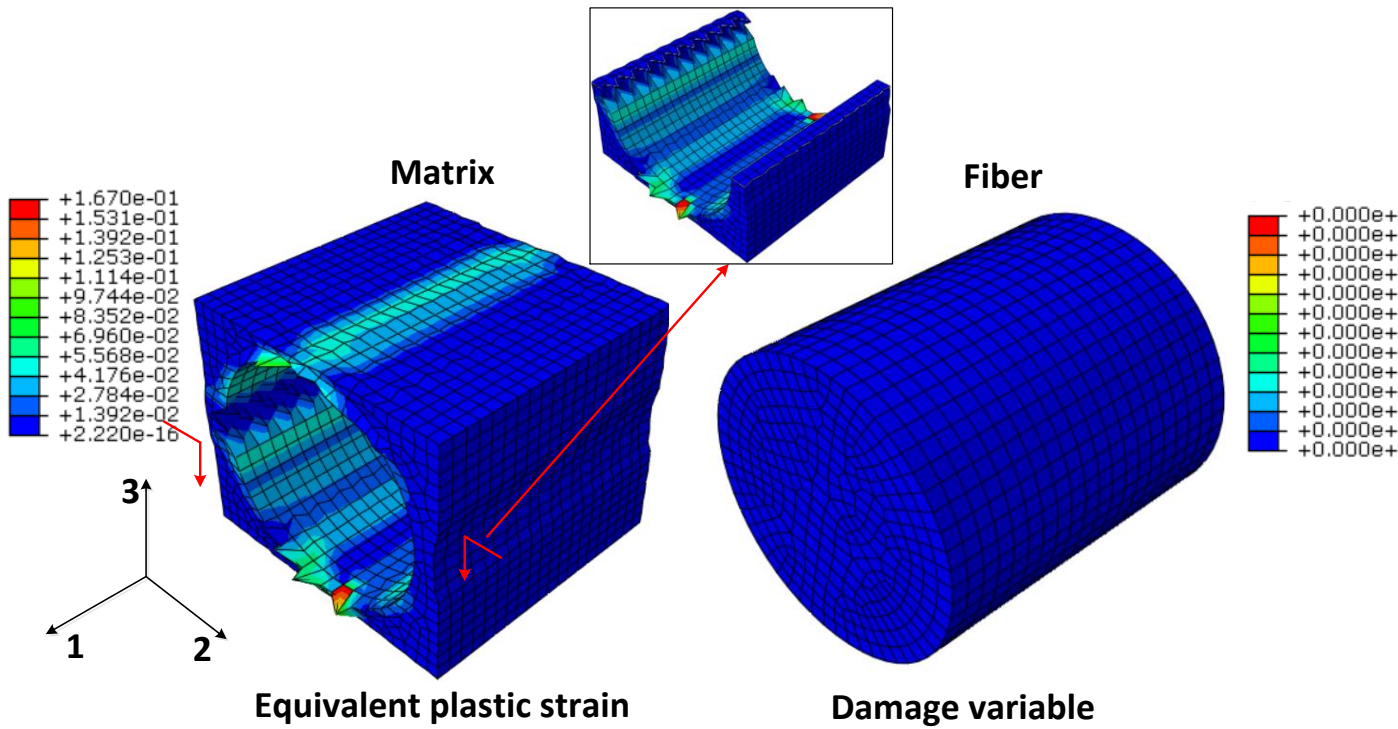
(b) Stress-strain curve comparisons

Figure (15): Transverse compressive behavior comparison



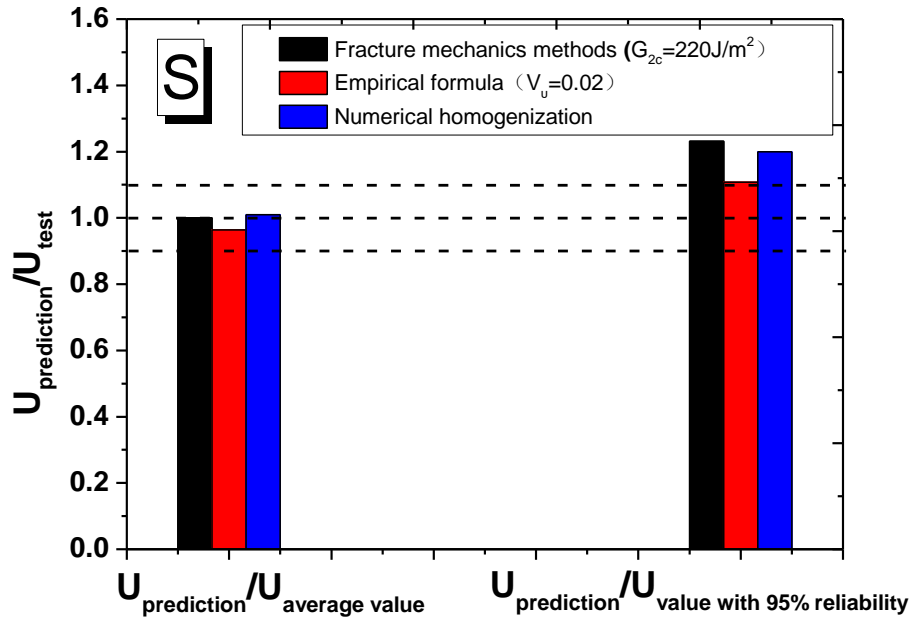


(a) Mises stress

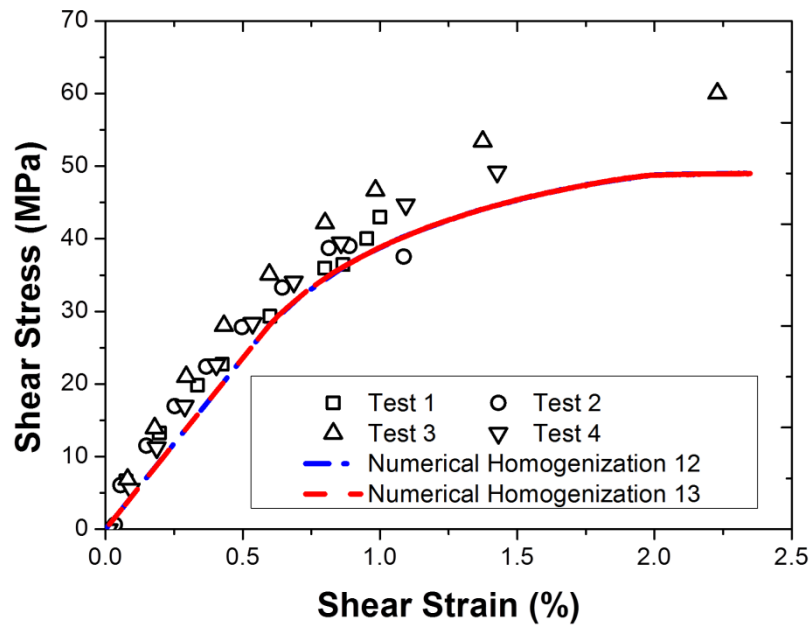


(b) Equivalent plastic strain and damage variable

**Figure (16):** Stress, plastic strain and damage distributions of unit cell under transverse compressive loading (33 direction)

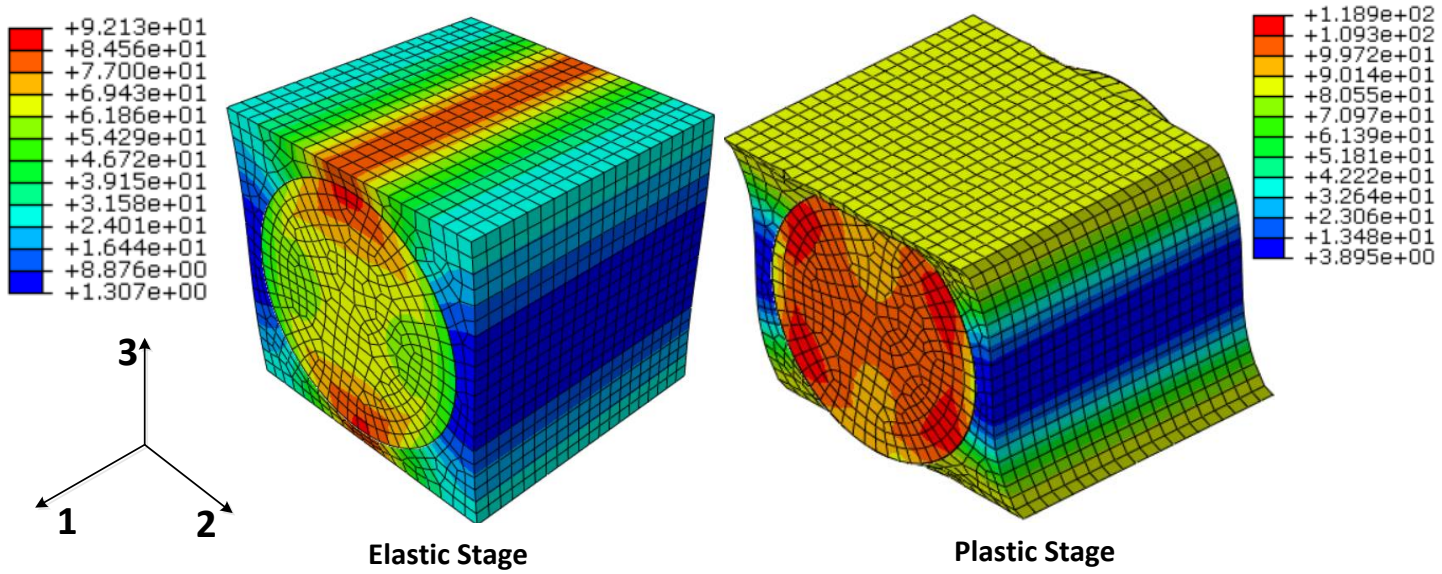


(a) Ultimate strength comparisons

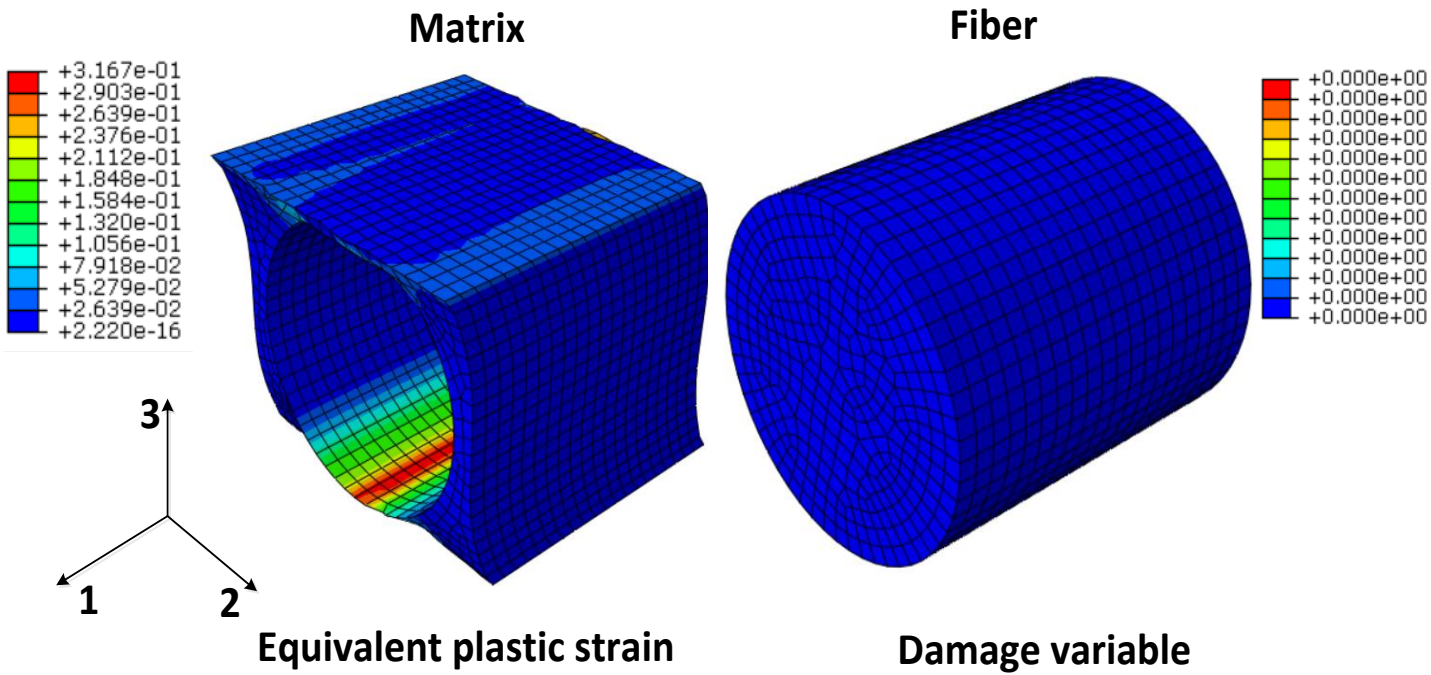


(b) Stress-strain curve comparisons

**Figure (17):** In-plane shear behavior comparison



(a) *Mises stress*



(b) *Equivalent plastic strain and damage variable*

**Figure (18):** Stress, plastic strain and damage distributions of unit cell under in-plane shear loading (*13*-direction)

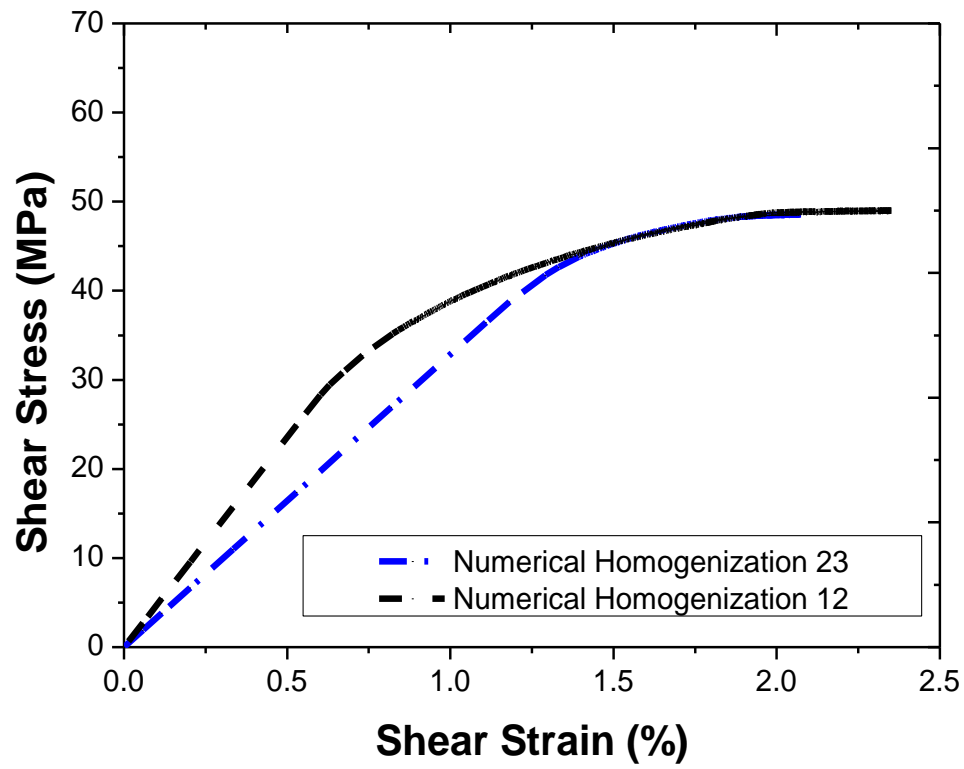
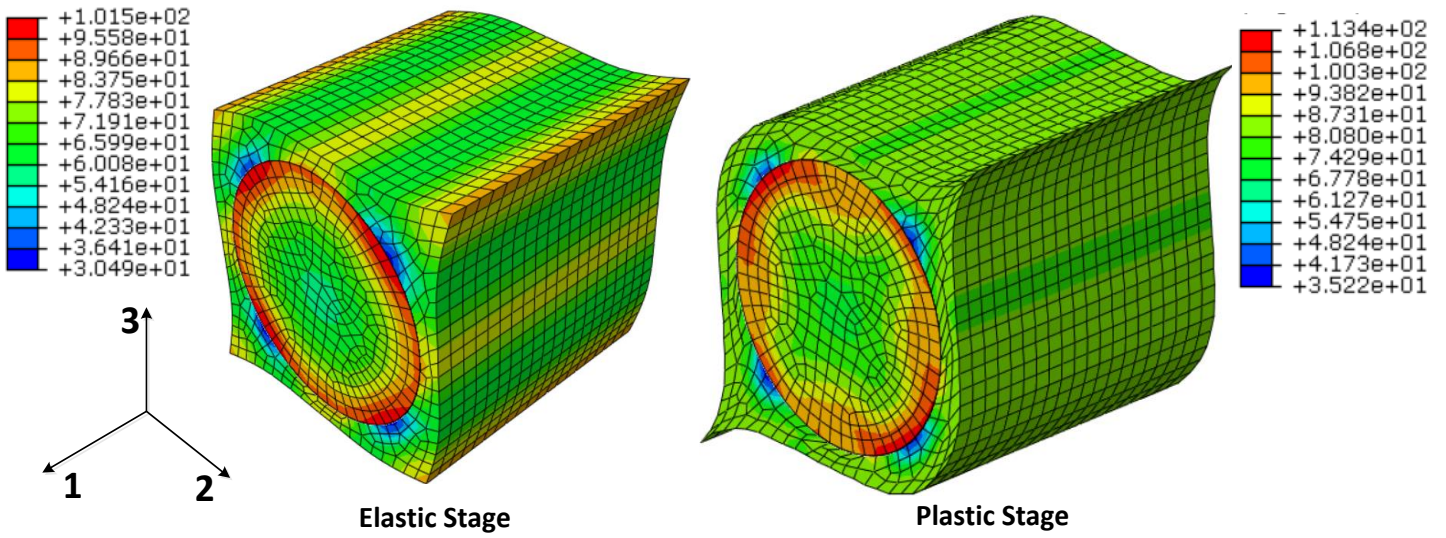
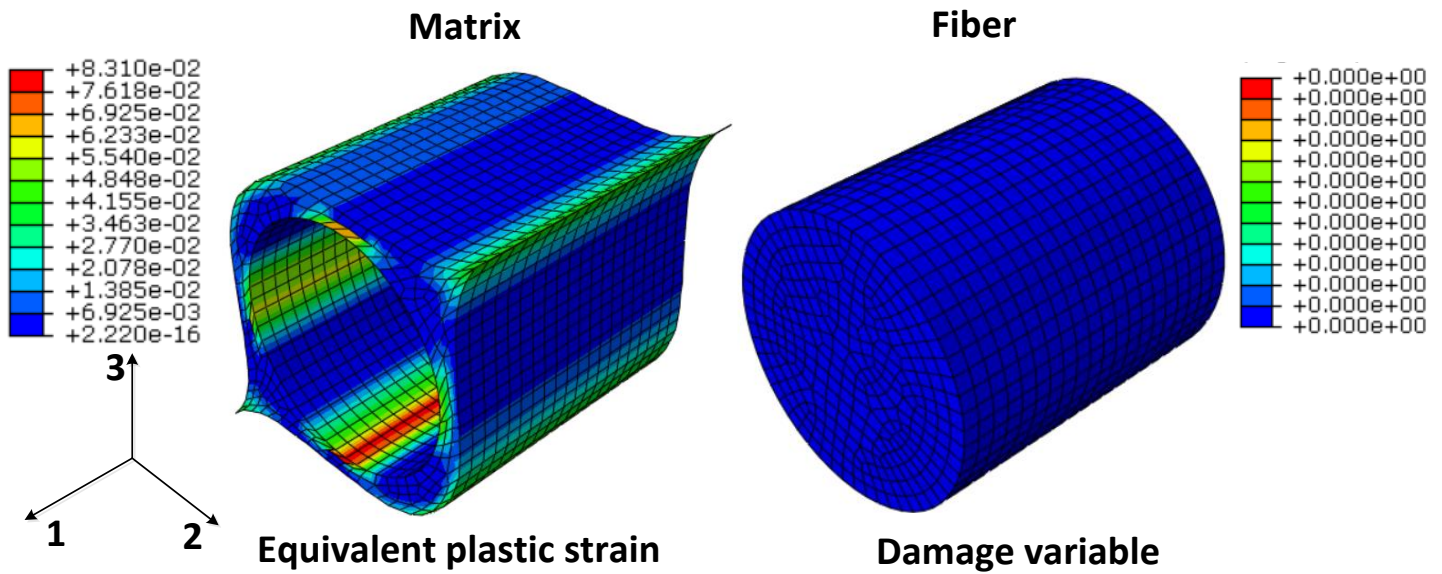


**Figure (19):** Transverse shear stress-strain curve



(a) *Mises stress*



(b) *Equivalent plastic strain and damage variable*

**Figure (20):** Stress, plastic strain and damage distributions of unit cell under transverse shear loading (23-direction)

## LIST OF TABLES

**Table 1:** Implementation algorithm of fiber damage model

**Table 2:** Mechanical properties of E-glass fibers

**Table 3:** Mechanical properties of epoxy resin

**Table 4:** Fiber volume fraction experimental results

**Table 5:** Summary of experimental results

**Table 6:** Summary of resistance factors

**Table 1:** Implementation algorithm of fiber damage model

1 Initial variable:  $\{ {}^n w, {}^n w^v, {}^n r \}$

2 Update strain:  ${}^{n+1} \varepsilon_i = {}^n \varepsilon_i + \Delta \varepsilon_i \quad i = 1 \dots 6$

3 Compute the principal strain  ${}^{n+1} \bar{\varepsilon}_j \quad j = 1 \dots 3$

4 Compute the equivalent strain  ${}^{n+1} \hat{\varepsilon}$

5 Update stress and Jacobian Matrix:

5-1 If  ${}^{n+1} \hat{\varepsilon} \leq {}^n r$  :

$${}^{n+1} r = {}^n r, {}^{n+1} w = {}^n w, {}^{n+1} w^v = {}^n w^v$$

5-2 If  ${}^{n+1} \hat{\varepsilon} > {}^n r$  :

$${}^{n+1} r = {}^{n+1} \hat{\varepsilon}, {}^{n+1} w = \Upsilon({}^{n+1} \hat{\varepsilon})$$

$${}^{n+1} w^v = \frac{\eta}{\eta + \Delta t} {}^n w^v + \frac{\Delta t}{\eta + \Delta t} {}^{n+1} w$$

5-3: Update Stress:

$${}^{n+1} \sigma_{ij} = (1 - {}^{n+1} w) L_{ijkl} {}^{n+1} \varepsilon_{kl}$$

5-4: Update Jacobian Matrix:

$${}^{n+1} \left( \frac{\partial \sigma_{ij}}{\partial \varepsilon_{kl}} \right) = (1 - {}^{n+1} w) L_{ijkl}$$

**Table 2:** Mechanical properties of E-glass fibers

Longitudinal modulus, $E_{f1}$ (GPa)	Transverse modulus, $E_{f2}$ (GPa)	Poisson's ratio, $\nu_f$	Shear modulus, $G_f$ (GPa)	Tensile strength, $X_{ft}$ (MPa)	Compressive strength, $X_{fc}$ (MPa)	Density, $\rho$ (kg/m <sup>3</sup> )
74.0	74.0	0.20	30.80	2,150	1,450	2,560



**Table 3:** Mechanical properties of epoxy resin

Modulus, $E_m$ (GPa)	Poisson's ratio, $\nu_m$	Shear modulus $G_m$ , (GPa)	Tensile strength $X_{mt}$ , (MPa)	Compressive strength, $X_{mc}$ , (MPa)	Shear strength, $S_m$ , (MPa)	Density( $\rho$ ), (kg/m <sup>3</sup> )
3.35	0.35	1.24	80.0	120.0	75.0	1,160

**Table 4:** Fiber volume fraction and density

Number	Length (mm)	Width (mm)	Thickness (mm)	Mass <i>before</i> burning, (g)	Mass <i>after</i> burning, (g)	Composite density, (kg/m <sup>3</sup> )	Fiber fraction (%)
1	24.12	25.11	4.2	4.84	3.65	1902.7	56.1%
2	24.95	23.93	4.05	4.05	3.50	1931.3	56.5%
3	25.00	23.47	4.22	4.22	3.55	1926.4	56.0%
<b>Average</b>						<b>1,920.1</b>	<b>56.2%</b>

**Table 5:** Summary of test results

Property	Number	Elastic Modulus (GPa)				Ultimate Strength (MPa)			
		<i>SD</i>	<i>E<sub>av</sub></i>	<i>E<sub>95%</sub></i>	<i>COV</i>	<i>SD</i>	<i>U<sub>av</sub></i>	<i>U<sub>95%</sub></i>	<i>COV</i>
Longitudinal Tensile	5	3.10	47.17	43.12	0.07	33.93	1146.03	1104.50	0.03
Transverse Tensile	5	1.35	16.18	14.51	0.08	5.31	47.45	40.86	0.11
Longitudinal Compressive	5	0.96	55.02	53.82	0.07	70.83	1014.34	926.40	0.02
Transverse Compressive	5	0.06	16.74	15.45	0.06	3.49	168.40	164.20	0.02
In-plane Shear	5	0.46	5.04	4.55	0.09	8.47	48.50	39.38	0.10
Poisson's ratio	5	Longitudinal Poisson's ratio				Transverse Poisson's ratio			
		<i>SD</i>	<i>v<sub>xyav</sub></i>	<i>v<sub>xy95%</sub></i>	<i>COV</i>	<i>SD</i>	<i>v<sub>yxav</sub></i>	<i>v<sub>yx95%</sub></i>	<i>COV</i>
		0.017	0.265	0.286	0.06	0.011	0.114	0.128	0.10

**Table 6:** Summary of resistance factors

<b>Property</b>	<b>95% Reliability</b>		<b>99% Reliability</b>	
	<i>Elastic Modulus</i>	<i>Ultimate Strength</i>	<i>Elastic Modulus</i>	<i>Ultimate Strength</i>
Longitudinal Tensile	0.88	0.95	0.84	0.93
Transverse Tensile	0.87	0.82	0.81	0.74
Longitudinal Compressive	0.88	0.97	0.84	0.95
Transverse Compressive	0.90	0.97	0.86	0.95
In-plane Shear	0.85	0.84	0.79	0.77
Longitudinal Poisson's ratio	0.90	--	0.86	--
Transverse Poisson's ratio	0.84	--	0.77	--